Nanoscale

PAPER

View Article Online
View Journal

Cite this: DOI: 10.1039/d5nr00915d

Molecular insight into the efficient & robust design of vesiculated protein nano-cages

Shadi Rahnama [a] and Mohammad Reza Ejtehadi *[b]

Received 2nd March 2025,
Accepted 2nd November 2025

DOI: 10.1039/d5nr00915d

rsc.li/nanoscale

Recently, recapitulation of viromimetic function in non-viral protein nanocages (PNCs) has emerged as a strategy to successfully encapsulate them in membrane vesicles. This method successfully evaded immune system detection. The mechanism responsible for triggering membrane budding and vesiculation remains elusive. This is primarily because the membrane initially interacts with flat protein arrangements from nanocages (whether pyramidal, dodecahedral, or icosahedral), and it is unclear how these seemingly flat arrangements can overcome the inherent mechanical resistance of the lipid bilayer to induce curvature. In this study, we considered a trimeric interface of a dodecahedron nanocage and explored the energetic and molecular role of its viromimetic module in protein nanocage packaging. Using a combination of all-atom and MARTINI coarse-graining molecular dynamics, we show that a stronger highly basic region (HBR) promotes electrostatic sequestration of PIP2 lipids, known for their larger headgroups, to accumulate around trimer binding sites, forming a PIP2 depletion zone in the central region of the trimer interface. Such lipid-sorting events resulted in membrane thickness distributions with taller lipids accumulating toward the margins and shorter ones at the center of the trimer and inducing curvature to the lipid bilayer due to stretching and contraction in different regions of the lipid interface. Our findings give molecular-level mechanistic insights into curvature generation and propagation in membranes induced by engineered PNC interactions, as well as a generic molecular design approach for clathrin-independent nanoparticle exocytosis.

1 Introduction

Protein nanocages hold immense promise for targeted drug delivery and immunologically stealthy therapeutics. A significant challenge hindering their clinical translation is the inefficient and uncontrolled encapsulation of these nanocages within membrane vesicles – vesiculation. To overcome this hurdle, researchers are increasingly turning to nature for inspiration, particularly to the elegant strategies employed by viruses for membrane manipulation and self-assembly. Years of research on viral replication and pathogenic pathways have yielded valuable insights into viral function.[1] Viruses employ an intrinsic mechanism to safeguard their genetic material, transport it to the extracellular space, evade immune responses upon entering target cells *via* interactions with receptors, and deliver it into the cell compartment. Through this process, they exploit self-assembled and distinctive protein structures known as capsids, which possess the capability to interact with host cells.[2]

The capsid structure of viruses epitomizes the principles of protein self-assembly in nature. Structural analysis reveals that this protein shell comprises a specific number of subunits that envelop and safeguard the viral genome.[3] Viral capsids possess inherent programming to target and penetrate host cells, evolved to facilitate nucleic acid exchange across different chemical environments.[4]

Regarding their chemical and physical properties, capsids or natural nanocages exhibit stability against environmental pressures while remaining sensitive to signals or changes in the cellular environment, enabling the release of their cargo into the target microenvironment.[5,6] The notable attributes of protein nanocages, including biocompatibility, functional diversity, biological manufacturing, and design flexibility through protein engineering, make them potent structures for various applications.[7]

To date, viral capsids have found specialized applications. For instance, capsid bacteriophages are utilized in peptide display technology for synthesizing receptors for specific proteins, filamentous phages serve as templates for nanomaterial synthesis, and virus-like particles (VLPs) are employed in vaccine production, targeted drug delivery to cells, and the creation of bionanoreactors for material synthesis.[7]

Despite the distinctive attributes of viruses, continuous efforts persist to manipulate their protein sequences for the

[a]Institute for Convergence Science & Technology, Sharif University of Technology, Tehran, 14588, Iran. E-mail: sh.rahnama251@sharif.edu
[b]Department of Physics, Sharif University of Technology, Tehran, 14588, Iran. E-mail: ejtehadi@sharif.edu

incorporation of novel or supplementary functionalities. Recent investigations have kindled optimism regarding the enhancement of nanocage architecture through the development of synthetic peptide sequences capable of self-assembling into structured protein nanocages.[8–11] Analogous to their natural counterparts, peptide aggregation in these synthetic constructs arises from a diverse array of non-covalent interactions.[12] To enhance the utility of synthetic protein nanocages in diagnostic and therapeutic realms, as well as to modulate immune responses, they have been conjugated with diverse moieties, including sugars, lipids, nucleotides, and polymers, yielding hybrid protein scaffolds.[13]

For instance, in recent research inspired by viral counterparts of synthetic protein nanocages, researchers introduced a modular method for conjugating structured nanocages with lipid membranes.[14] By emulating viruses that are encapsulated within lipid membranes, it is proposed that three fundamental capabilities must exist in the genetic design of any functional nanocage, conferring upon it the ability to be released into membrane vesicles, namely:

1. Possibility of binding to the membrane (to overcome the energetic barrier required for membrane curvature induction)
2. Self-structuring
3. Utilization of the ESCRT machinery to induce membrane curvature during the final stages of budding

In a test case, membrane binding capability is conferred by incorporating a sequence of six basic amino acids derived from the *N*-myristoylated Gag structure of the HIV. Furthermore, a polypeptide consisting of 52 residues from Gag p6 was utilized to introduce membrane curvature induction in the final step. The test case is vesiculated, and despite the innovative concept and evaluation with diverse membrane binding and late budding machinery from various viruses, it yielded mixed results. In certain instances, combinations of genetic codes led to the encapsulation of 15 or more nanocages within a single vesicle, while in others, fewer nanocages were encapsulated. However, consistent encapsulation of a specific number of nanocages within vesicles was not observed in any instance.[14] Precise control over nanocage encapsulation is imperative for therapeutic applications, underscoring the need to elucidate the underlying causes.

The proposed technique, using a natural coating for administered agents and relying on single-celled self-organization for production, promises a distinctive position among drug packaging tools. Understanding the roles of viruses in origin of life scenarios[15,16] and genetic mutation[17–19] further motivates biomimetic approaches. Achieving artificial structures mimicking their natural counterparts could lead to unprecedented scientific advancements and deeper natural understanding.

Many studies have explored the formation of inward tubular invaginations, predominantly focusing on proteins with homogeneous shapes characterized by high curvature, such as spheres, caps, cylinders, and ovals.[20–30] In contrast, nanocages often possess outer surfaces that are largely hollow, and their interacting surfaces with membranes are typically flat, unlike the aforementioned geometries. Furthermore, it should be noted that previous research did not always consider the atomic details of proteins. In this article, however, we emphasize the molecular structure of nanocages as a crucial element in understanding the mechanism of membrane curvature. While the broad involvement of lipid composition and lipid sorting in membrane remodeling has been established,[31,32] the detailed molecular underpinnings of how these phenomena translate into curvature for geometrically flat protein assemblies remain less explored.

The nanocage in this study is a synthetic dodecahedron,[11] with a consistently flat, hollow pentagonal interface (Fig. 1). Each pentagonal structure comprises five trimers, with each trimer located at a vertex. Given that the bending rigidity of the nanocage is higher than that of the lipid bilayer,[11,14] understanding the specific effects of each trimer on the membrane is crucial for addressing their cooperation in inducing membrane curvature. Therefore, elucidation of the underlying mechanism of invagination can be accomplished by investigating the induction mechanism of the system's smallest building block: the trimers. These trimeric protein scaffolds possess a completely flat configuration and they are positioned at the corners of a pentagon (Fig. 1a). In this study, we explore the significance of this spatial arrangement of trimers in the formation of vesiculated nanocages. To elucidate the curvature mechanism, we utilized coarse-grained and all-atom molecular dynamics simulations, which revealed that lipid sorting is the primary cause of membrane curvature by these flat structures. This process hints at the use of biophysical 'cheap tricks' – an energy-efficient strategy that leverages the natural propensity of lipids to self-reorganize without substantial energy

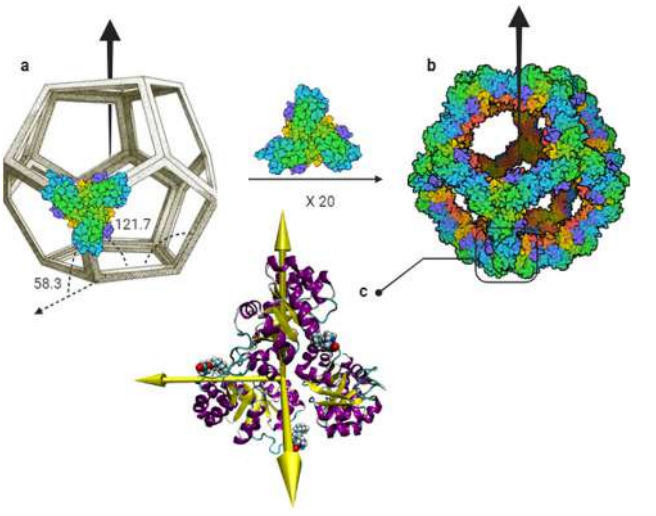

Fig. 1 (a) Synthetic dodecahedron and an aligned trimeric building block, showing the angles of the landing surface in relation to the interface. (b) A complete nanocage composed of 20 trimeric building blocks. (c). Atomistic detail of a trimeric building block. Positioning at 58.3 degrees in relation to the interface places its lipid tail in a trigger position for anchoring to the lipid bilayer. The yellow axes are principal axes of the trimer.

input.[33,34] While the concept of lipids segregating into domains of preferred curvature is known,[31] our simulations reveal the precise molecular events by which this sorting, driven by electrostatic interactions, leads to localized variations in membrane thickness. This sorting involves attracting longer lipids to the trimer corners and organizing shorter lipids in the interstitial spaces.

2 Materials and methods

The initial coordinates of the protein nanocage were derived from PDB entry 5KP9. Unresolved amino acids, due to the low resolution (5 Å) of electron microscopy, were simulated using Modeller[35] in Chimera[36] and incorporated into the original structure. The N-terminal region, which interacts with the membrane, includes a lipid tail. Five different approaches were used to modify the charge and lipidation state of the N-terminal region utilizing VMD[37] software and TCL[38] scripts. In model I (Fig. 2), a myristic acid tail was added to the N-terminal, following the model proposed by Vottler;[14] this serves as our native model, with the other models generated for comparison. In model II (Fig. 2), the myristic acid tail was replaced by a palmitic acid lipid chain. Model III (Fig. 2) retained the myristoylation signal, as in model I, but the first five amino acids of the HIV-1 Gag protein were replaced with a poly-positive lysine (K4) chain to introduce a strong positive charge. Models IV and V were designed to explore the role of an additional lipid tail at the N-terminal binding site. Model IV (Fig. 2) included an extra myristic acid tail at glycine14, compared to model I, while model V (Fig. 2) was identical to model IV except that the 2–6 Gag sequence was replaced with a poly-neutralized alanine sequence. The H++ algorithm[39] was used to estimate the pK_a values of ionizable amino acids in the protein at physiological pH. The calculated values indicated that all nine histidines present in the protein adopt a neutral protonation state. The lipid membrane was constructed using the Charm-GUI online platform.[40] The lipid composition was modeled to reflect the proportions observed in the HIV virus capsid, specifically 20% PIP2, 13% POPC, and 67% POPE.[41] A detailed rationale for this lipid composition and the equilibration strategy, including the initiation of simulations within physiologically relevant, pre-enriched microdomains, is provided in Appendix A.3. The membrane was constructed with dimensions of 10 × 10 nanometers. The corresponding image, along with the structures of the constituent lipids, is presented in Fig. 3.

2.1 CG model

The simulations employed the MARTINI coarse-grained force field, version 2.x, and its extensions. Specifically, the protein trimers were mapped into a CG representation based on the original MARTINI force field,[42,43] incorporating modifications for proteins as described by Shih and colleagues.[44] These protein parameters are consistent with subsequent MARTINI 2.x protein force field refinements.[45,46] To preserve the secondary and tertiary structures of the proteins,[47] an elastic network

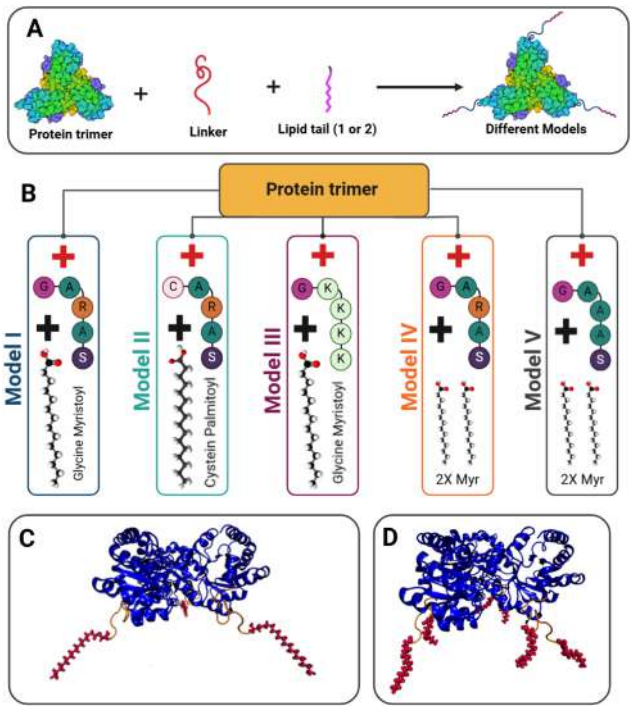

Fig. 2 (A) Five different models of protein modification used in this study, created by adding a linker and one or two lipid tails to the primary protein trimer. (B) Atomistic differences between the models: model I includes a single myristic acid tail at the N-terminal and serves as the native model, with the linker sequence identical to the 2–6 HIV-1 Gag peptide sequence. Model II replaces the myristic acid tail with a palmitic acid chain. Model III retains the myristic acid tail but introduces a strong positive charge by replacing the 2–6 Gag sequence with a poly-lysine (K4) chain. Model IV adds a second myristic acid tail at glycine14, while model V is similar to model IV but replaces the 2–6 Gag sequence with a poly-alanine sequence, neutralizing the charge. (C) All-atom representation of model III (the first three models are almost identical to this model in appearance, disregarding the details). (D) All-atom representation of model IV (model V is almost identical to this model in appearance, disregarding the details).

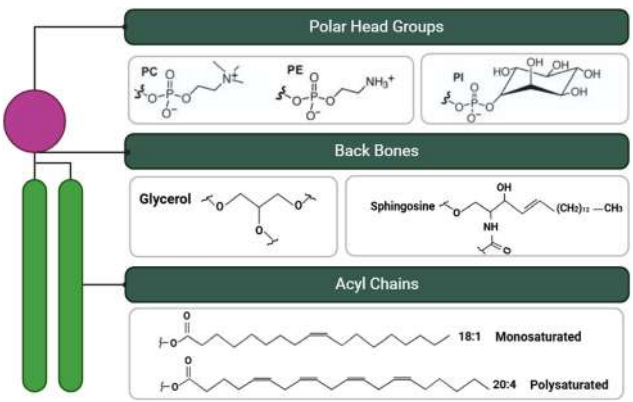

Fig. 3 Structural representation of lipids used in this study. The lipids differ in their acyl chain length and degree of saturation: the monounsaturated lipids (POPC, POPE) contain 18-carbon acyl chains, while the polyunsaturated PIP2 lipids feature longer 20-carbon acyl chains. Also the larger polar head group is characteristic of PIP2 (phosphatidylinositol 4,5-bisphosphate).

model was applied with a constant force of 0.597 kcal (mol Å^2)$^{-1}$ between BAS beads separated by distances in the range of 4 Å to 10 Å, excluding the first 24 N-terminal residues (GLY-2 to LYS-25). The lipid parameters for POPC, POPE, and PIP2, including coarse-grained (CG) representations for the aliphatic moieties of the Myr and Pal groups, were directly adopted from the SI of Charlier *et al.* (2014),[48] which provides specific parameters consistent with MARTINI 2.x lipid parameterizations.[49,50] This ensures a consistent force field environment for all components.

Water molecules, antifreeze particles, and counter-ions were added separately to each component of the system (membrane and protein trimers), which were equilibrated individually for 1 μs. Following equilibration, the systems were combined, with each protein model placed 12 Å away from the surface of the membrane. It should be noted that although initially placed 12 Å apart, the hydrophobic lipid tails of the protein trimers were spontaneously inserted into the membrane's hydrophobic core during the equilibration phase, establishing stable protein–membrane interactions prior to the production runs. Solvation and ionization were then performed for the combined systems, resulting in a simulation box with an approximate size of 120 × 115 × 145 Å and containing approximately 15 500 beads.

All coarse-grained simulations were carried out using the NAMD2.12 software.[51] Prior to the production simulations, the final structures of all models were minimized for 5000 steps to eliminate any steric clashes. Periodic boundary conditions were applied under the NPT ensemble. Temperature was maintained at 310 K using the Langevin thermostat (damping coefficient of 5 ps). Pressure was maintained at 1.01325 bar (approximately 1 atm) using the Langevin Piston method, with a Langevin Piston Period of 2000 fs and a Langevin Piston Decay of 1000 fs. The simulation cell was set to be flexible with a constant ratio between its dimensions, allowing for volume fluctuations while preserving relative box dimensions. The Langevin thermostat damping coefficient was set to 5 ps, with a barostat time constant of 1000 fs and a collapse time constant of 500 fs. A time step of 10 fs was used throughout the simulations. Non-bonded interactions, including both Lennard-Jones and electrostatic interactions, were calculated with a cutoff distance of 12.0 Å and a 1–2 exclusion. A switching function was applied, where interactions began to smoothly decay to zero at a switch distance of 9.0 Å. The dielectric constant was set to 15.0, and the Particle Mesh Ewald (PME) method was not used, consistent with standard MARTINI force field practices for coarse-grained systems.

For each model, three replicas were simulated, each undergoing unconstrained evolution for approximately 0.5 μs. The simulation results were analyzed using VMD software and custom Python scripts. Throughout the manuscript, error bars, representing the standard deviation across all three independent replicas, are consistently shown as shaded regions around the mean lines in time evolution plots.

While the MARTINI coarse-grained force field, like any coarse-grained model, has inherent limitations (*e.g.*, in capturing subtle lipid tail packing differences or potential overestimation of certain clustering phenomena), it remains a powerful tool for simulating large-scale membrane dynamics and protein–lipid interactions driven by strong electrostatic and steric effects, which are central to our proposed mechanism. Specifically, while the MARTINI force field has previously been shown to be "too 'sticky' for the interactions of globular proteins in aqueous solution",[52] simulated protein–lipid interactions[53,54] and protein–protein interactions within the lipid bilayer[55–57] seem to reproduce experimental results quite well.[58] This provides substantial confidence that the lipid–lipid clustering and protein–lipid interactions observed in our simulations, driven by the strong electrostatic attraction between the protein's HBR and PIP2, are not merely artifacts of the CG model.

2.2 All-atom model

All-atom simulation was performed for free energy calculation. All-atom setups for model I were obtained by reverse mapping from its coarse-grained MARTINI model, utilizing the CHARMM-GUI's CG-to-all-atom conversion feature, a methodology extensively documented in the VMD CGTools webpage.[59] Subsequently, the backmapped structure underwent a simulated annealing protocol to ensure thermal equilibration. While the primary coarse-grained simulations were conducted at 310 K, this annealing step was crucial for smoothly transitioning the all-atom system from potentially non-equilibrium configurations and high initial kinetic energies, introduced post-backmapping and velocity reinitialization, to the target physiological temperature. The NAMD configuration file specified initial velocity randomization at 610 K using the 'reinitvels' command. The annealing process, governed by the 'reassignTemp' parameter, then involved a controlled, gradual decrease in temperature (*e.g.*, from 610 K down to 300 K). This systematic cooling mitigated kinetic energy fluctuations and structural instabilities, thereby ensuring a robust and stable starting configuration for subsequent all-atom molecular dynamics. This comprehensive backmapping procedure, including its thermal equilibration and annealing steps, adheres to established recommendations by VMD CGTools and is often facilitated by NAMD configuration files automatically generated by these tools. The resulting structures were used as the initial configuration for all-atom modeling, with ten replicas designed for free energy calculations. Each system was solvated using the TIP3P water model and neutralized to 150 mM NaCl, resulting in a water box with an approximate size of 132 × 132 × 158 Å^3, containing around 192 000 atoms. CHARMM36m force field parameters[60] were applied, and molecular dynamics simulations were conducted using NAMD 2.12.[51] Periodic boundary conditions under the NPT ensemble maintained the temperature and pressure at 310 K and 1 bar, respectively, using the Langevin thermostat and Nosé–Hoover Langevin piston. A 12 Å cutoff was used for short-range van der Waals interactions, and long-range electrostatics were calculated *via* the Particle Mesh Ewald method. The R-RESPA multiple time step scheme, with a 2 fs time step, was used for integrating the equations of motion. Structures were minimized for 5000 steps to remove steric clashes, followed by equi-

libration: first for 0.5 ns in the NVT ensemble with restrained lipid tails, then for another 0.5 ns in the NPT ensemble under the same restraints. Given prior coarse-grained equilibrium, only an additional 1 ns of unrestrained all-atom modeling was necessary before performing free energy calculations.

2.3 Free energy calculation

The anchoring process of the trimer is typically accompanied by significant conformational changes in the protein. The total calculated potential of mean force (PMF) throughout the evolution of this process is composed of both the binding free energy of the protein to the lipid membrane and its associated conformational changes. To isolate the binding free energy component, we utilized the Collective Variables (colvars)[61] module in NAMD, which effectively reduces the protein's high-dimensional degrees of freedom into a manageable set of key parameters. By defining biasing potentials, we carefully modulated the system's dynamics in a controlled manner. In this study, we employed Steered Molecular Dynamics (SMD) to introduce biasing potentials, thereby enhancing sampling efficiency and facilitating exploration of the phase space along the reaction coordinate (Z). The reaction coordinate (Z) was precisely defined as the distance between the center of geometry (CoG) of the protein trimer and the midplane of the membrane, with its detailed calculation methodology provided in Appendix A.2.6. Each pulling trajectory for the Steered Molecular Dynamics (SMD) simulations commenced at an initial Z-distance of 50 Å and concluded at a final Z-distance of 80 Å. To ensure the statistical reliability and reproducibility of the free energy profiles, a total of ten independent pulling runs were performed for each system, with each run initiated from distinct initial configurations obtained after thermal equilibration. The protein trimer was pulled from the lipid membrane at a constant velocity of 0.0002 Å per timestep, with a virtual string attached to the protein's center of mass, and a force constant of 7.5 kcal (mol A^2)$^{-1}$ was applied. Simultaneously, a counteracting restraint (K = 20 kcal (mol $Å^2$)$^{-1}$) was applied to the phosphate groups of the lipid molecules to prevent membrane translocation in response to the biasing potential. The work performed during this non-equilibrium process is related to the equilibrium PMF *via* Jarzynski's equality,[62] given by:

$$\langle e^{-\beta W} \rangle = e^{-\beta \Delta F} \quad (1)$$

where $\beta = \frac{1}{k_B T}$, W is the work done on the system, and ΔF is the change in free energy. A detailed discussion on the theoretical underpinnings, convergence, and practical application of Jarzynski's equality in our simulations, including the rationale for our chosen pulling velocity and number of runs, can be found in Appendix A.2.3.

3 Results and discussion

Regardless of the membrane-binding motif, the majority of replica simulations reach an equilibrium state after 200 ns of simulation time, as indicated by the mean RMSD of each model (Fig. 18). In nearly all models, the mean RMSD stabilizes, reaching a plateau around 150 ns of simulation. Therefore, subsequent analyses were conducted post-equilibration.

To assess the impact of the motifs on each model's interaction with the membrane, we first evaluated the number of acyl tails inserted into the membrane. The methodology for quantifying lipid tail insertion is detailed in Appendix A.2.1. Model III exhibited the highest efficiency, with all three acyl tails inserting into the membrane on average across all replicas. In this model, the poly-positive lysine (K4) chain of the linker introduced the strongest charge in the membrane-binding motifs among the models, resulting in the strongest electrostatic interaction with the membrane. For models I and II, which incorporate the HIV-derived electrostatic motif, the average numbers of inserted tails were 2.33 ± 0.01 and 1.9 ± 0.02, respectively (Fig. 4).

In model IV, the tail attached to the first residue possesses an electrostatic motif similar to models I and II, whereas the tail on the eleventh residue is uncharged. Despite this, model IV achieved less success in membrane interaction compared to models I and II. Although an average of 2.06 ± 0.02 legs were observed to have been inserted (Fig. 4), this number represents less than 30 percent of the total six available tails. In contrast, other discussed models achieved over 60 percent insertion efficiency.

Specifically, the uncharged tail on the eleventh residue displayed significant fluctuations within the aqueous environment. Driven by hydrophobic interactions, this tail frequently associated itself with the first (charged) tail of the same protein monomer. The resulting complex then adhered to the external, more hydrophobic surfaces of the protein itself, effectively sequestering it from interacting with the lipid membrane (see appendix Fig. 22 for visual evidence). In some instances, this tangled complex was observed to be pulled into a hydrophobic cavity formed between adjacent monomers. This sequestration mechanism significantly reduced the overall insertion efficiency, leading to an average of only 2.06 ± 0.02 tail penetrations into the membrane for model IV (Fig. 4).

The situation worsened in model V, where the charged motif was replaced with a neutral series of alanines. Similar disruptions to those observed in model IV were also present, leading to an even lower average lipid tail insertion, dropping below one to 0.42 ± 0.01 (Fig. 4).

The overall results clearly indicate that the electrostatic charge of the membrane-binding motif at the N-terminus of the monomers significantly enhances the tail insertion phenomenon into the membrane.

Curvature induction analysis across different models reveals a spectrum of curvature-inducing capabilities, as quantified in Fig. 5. To visually exemplify this curvature induction, Fig. 6 illustrates the final snapshot of the system for model III, which exhibited the most pronounced curvature in our analysis. This snapshot reveals that the protein trimer in model III indeed induces a noticeable local curvature on the bilayer

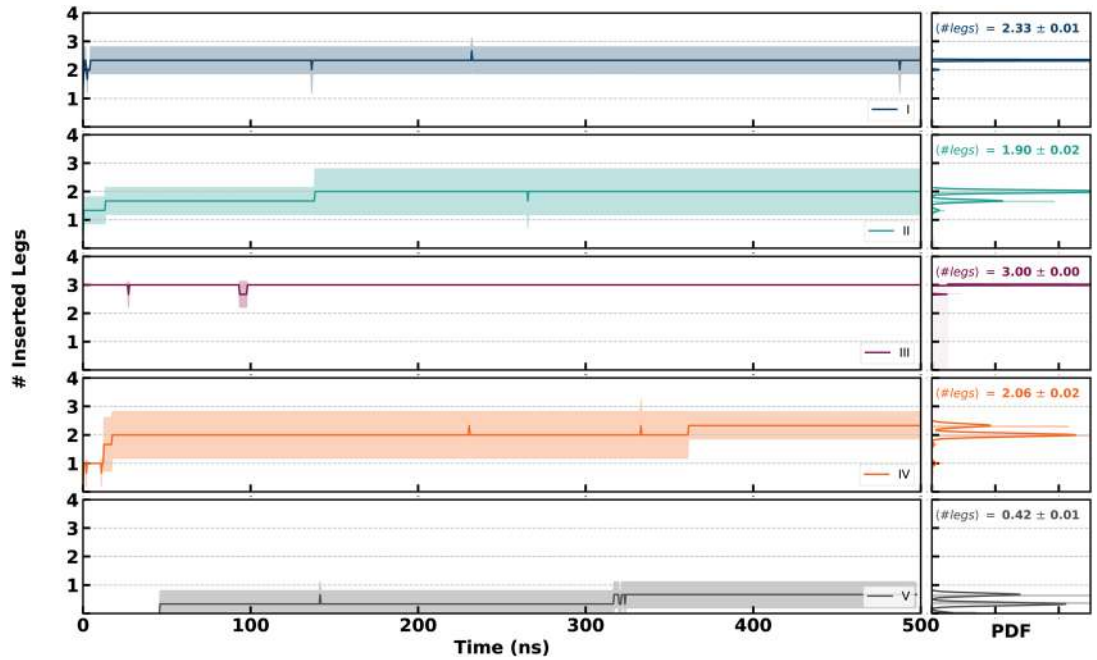

Fig. 4 Number of monomers in each model that successfully inserted at least one tail into the membrane over the simulation time. The left panels display the number of inserted tails (legs) as a function of time, while the right panels show the corresponding probability density functions (PDF) of the inserted tails for each model (I to V). The average number of inserted tails (⟨#legs⟩) is indicated for each model, highlighting variations in tail insertion dynamics across different systems.

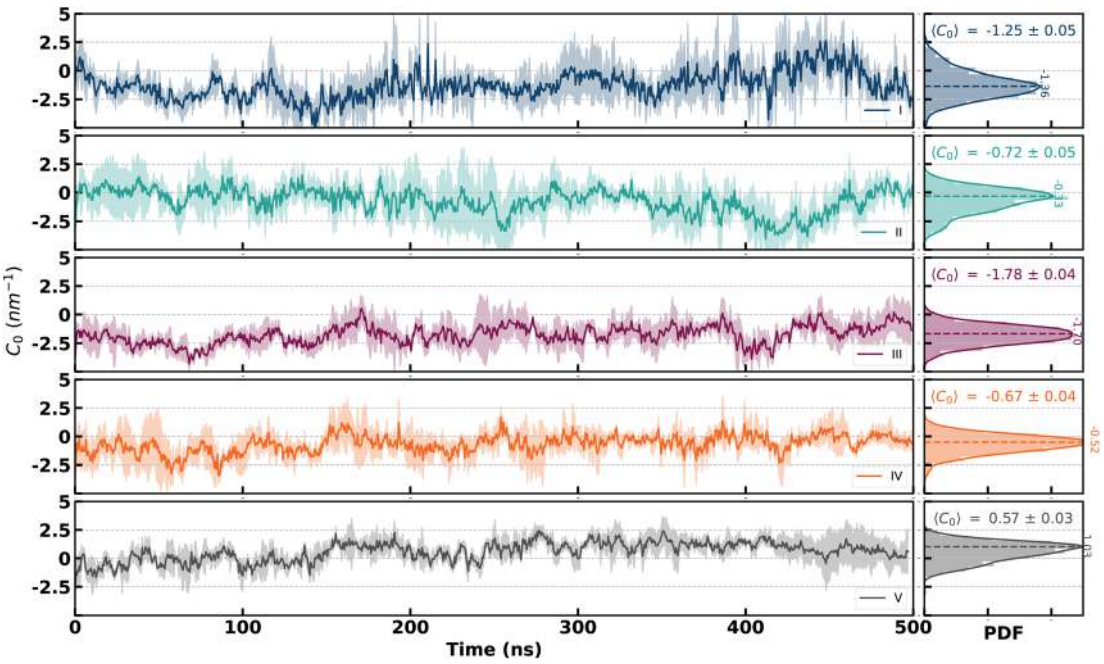

Fig. 5 Plot of local membrane curvature variations (C_0) over time in different protein models. Each subplot shows the time evolution of C_0 (left) alongside the corresponding probability density function (PDF) (right). The average curvature (⟨C_0⟩) is indicated for each model, revealing distinct curvature dynamics across the five protein models (I to V), with both positive and negative curvature trends observed.

surface. To provide a clearer depiction of this induced curvature, Fig. 6B presents the membrane surface fitted to a fifth-degree polynomial, as detailed in Appendix A.2.2.

Quantitative analysis of curvature induction (Fig. 5) illustrates that model III induces the most significant curvature in the membrane (⟨C_0⟩ = −1.78 ± 0.04 nm^{-1}), correlating with the

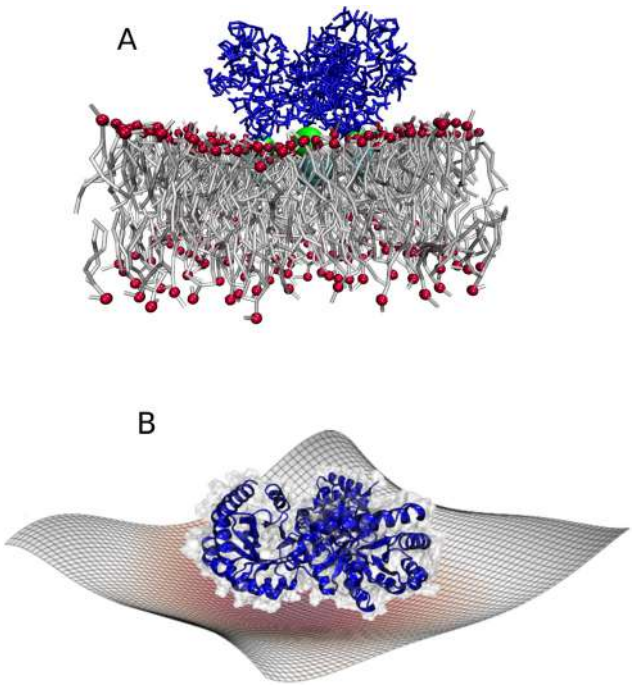

Fig. 6 (A) Membrane–protein complex inducing curvature in the membrane. (B) Visualization of the membrane surface showing the induced curvature more clearly, with the surface shape highlighted using polynomial fitting.

highest number of monomers successfully inserting their lipid tails into the membrane. This suggests that efficient penetration of monomers is a key driver of membrane deformation. In contrast, model V results in the lowest curvature ($\langle C_0 \rangle = -0.57 \pm 0.03\ \mathrm{nm}^{-1}$), indicating a weaker influence on the membrane structure, likely due to its minimal tail insertion (Fig. 4). This observation underscores the importance of monomer insertion in determining the extent of induced curvature.

Within this observed spectrum, models I and II represent intermediate levels of curvature induction. Model I exhibits a more pronounced curvature of $\langle C_0 \rangle = -1.25 \pm 0.05\ \mathrm{nm}^{-1}$, while model II shows a shallower curvature of $\langle C_0 \rangle = -0.72 \pm 0.05\ \mathrm{nm}^{-1}$. Correspondingly, model I achieves a higher average number of tail insertions into the membrane (2.49 ± 0.02 insertions) compared to model II (1.9 ± 0.02 insertions). This observed correlation between the number of inserted tails and the magnitude of induced curvature is consistent with expectations, further supporting the role of tail insertion as a primary mechanism for membrane deformation.

Model IV shows a relatively lower curvature ($\langle C_0 \rangle = -0.67 \pm 0.04\ \mathrm{nm}^{-1}$), which correlates well with its reduced capacity for tail insertion. This model, along with model V, clearly demonstrates that insufficient penetration of lipid tails into the membrane directly leads to a decrease in membrane deformation.

Overall, our results show that the degree of induced curvature is directly linked to the inserted tail stoichiometry. However, the mechanism by which tail insertion into the membrane induces curvature remains unclear. To gain a deeper understanding of the underlying molecular mechanism of curvature induction, we next investigated the correlative behaviour of membrane-interacting motifs of proteins and lipids of the membrane.

To investigate the correlative behavior of membrane-interacting motifs of proteins and lipids, we calculated the distribution function of the presence of the protein's "membrane-binding motifs" and PIP2 lipids in the *XY* plane (Fig. 7). For visual clarity and to highlight typical patterns, Fig. 7 shows a representative heatmap derived from one independent simulation replica per model; qualitatively similar distributions were consistently observed across all replicas. The methodology for generating these 2D probability density maps is detailed in Appendix A.2.4. In Fig. 7, the probability distribution of the presence of PIP2 molecules is presented in the left panels, while for the protein's binding motifs, it is in the right ones. Preliminary analysis of Fig. 7 reveals a distinct spatial correlation between these two quantities. For instance, in model III, three prominent orange-reddish regions are visible at the centers (0, 20), (0, −20), and (0, 40) in the right panel, representing highly probable regions for protein motif insertion. These regions coincide with the high-probability regions of the presence of PIP2 in the left panel. Seemingly, these hotspot regions of protein motifs act as absorption points for PIP2 lipids, leading to areas with a high probability of the presence of PIP2 (PIP2-enriched regions) in the left panel. Conversely, colder-colored regions in the left panel indicate areas that appear to be depleted of PIP2 lipids. This pattern is observed to varying degrees across other models as well. However, it remains unclear whether this relationship between protein and membrane components is consistent across different systems.

To address this question, we defined a metric called the "relative probability" ($f_{\tau\phi}$) to quantify the overlap between the distributions of the motifs and PIP2 lipids on the membrane surface:

$$f_{\tau\phi} = \frac{\iint \tau(x,y)\phi(x,y)\mathrm{d}x\mathrm{d}y}{\iint \tau(x,y)\mathrm{d}x\mathrm{d}y \times \iint \phi(x,y)\mathrm{d}x\mathrm{d}y}. \quad (2)$$

Here, $\tau(x, y)$ represents the probability distribution of the motifs and $\phi(x, y)$ represents the probability distribution of PIP2 lipids. This formula measures the degree of co-localization between the motifs and PIP2 lipids. A higher value of $f_{\tau\phi}$ indicates a stronger spatial correlation, implying more effective formation of absorption points, while a lower value indicates the opposite. Detailed computational procedures for generating $\tau(x, y)$ and $\phi(x, y)$ (*e.g.*, using kernel density estimation, grid size, and normalization) and calculating $f_{\tau\phi}$ are provided in Appendix A.2.5.

To ensure the validity and physical relevance of the $f_{\tau\phi}$ metric in relation to stable curvature induction, only simulation replicas where more than one lipid tail was observed to have been inserted into the membrane were considered for its calculation. Initial observations revealed that in cases with one or fewer tail insertions, the $f_{\tau\phi}$ value exhibited an artificial increase, decoupling it from the overall membrane curvature

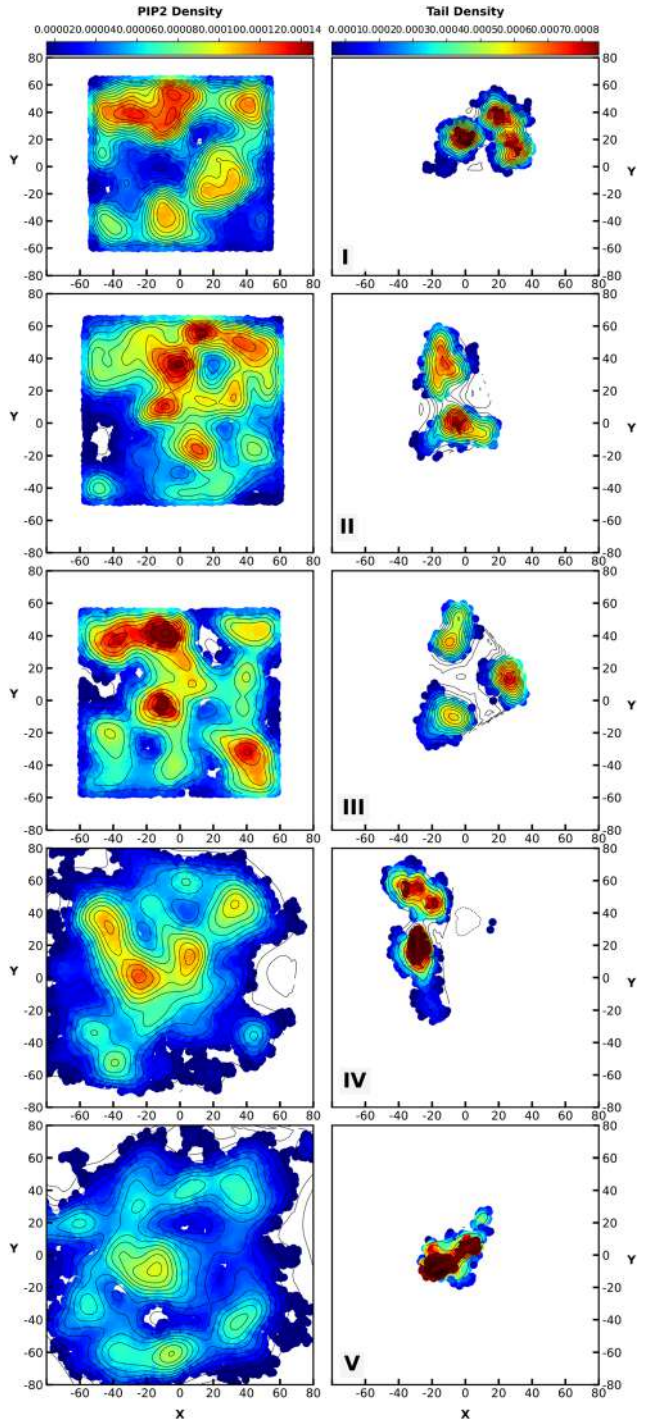

Fig. 7 Probability distribution of PIP2 molecules (left) compared to the probability distribution of protein tail insertion (right) into the membrane surface for different models. The color scale represents the probability density, with red regions indicating higher density and blue regions indicating lower density. The spatial correlations between the presence of PIP2 lipids and tail insertion points suggest a significant relationship across different models.

and thus rendering its correlation with induced curvature unreliable. This filtering criterion is crucial for maintaining the robustness of our subsequent analysis.

To quantify the correlation between the induced curvature (C_0) and the relative probability ($f_{\tau\phi}$), we plotted the scatter plot of these variables in Fig. 8. The horizontal axis represents the induced curvature, while the vertical axis shows $f_{\tau\phi}$. Each point on the scatter plot corresponds to a specific model, indicating the values of both variables. The data suggest that as the induced curvature becomes more negative, the value of $f_{\tau\phi}$ tends to increase.

Performing linear regression on the data yielded a correlation coefficient of corr(C_0, $f_{\tau\phi}$) = −0.94 and a p-value of 0.0586 (Fig. 8), further confirming the strong inverse relationship between these variables and the consistent correlation between the probability of the presence of protein motifs and PIP2 lipids across different models. Consistent with the aforementioned filtering criterion, model V, which consistently failed to achieve significant lipid tail insertion across its replicas, was excluded from this correlation analysis. This exclusion ensures that the correlation is drawn from models exhibiting a range of productive membrane-interaction mechanisms, thereby enhancing the robustness of our findings and allowing for a clearer understanding of the underlying principles of curvature induction.

A closer examination of the molecular structures of the PIP2-enriched and PIP2-depleted regions brings us closer to identifying the underlying reason for the formation of this correlation. As depicted in Fig. 3, PIP2 lipids feature multi-unsaturated acyl chains composed of 20 carbon atoms, whereas POPC and POPE have shorter chains with 18 carbon atoms, with POPC being saturated and POPE monounsaturated. In typical phospholipids like POPC, the glycerol backbone is oriented approximately perpendicular to the membrane plane, while the head group lies parallel to it.[63] In contrast, the PIP2 head group aligns perpendicularly with respect to the membrane.[64,65] The notable size and potentially upright structure of the PIP2 head group suggest that it may protrude more prominently into the aqueous phase compared to other phospholipids. These properties collectively make PIP2 "taller" than other membrane lipids. Its unique headgroup structure

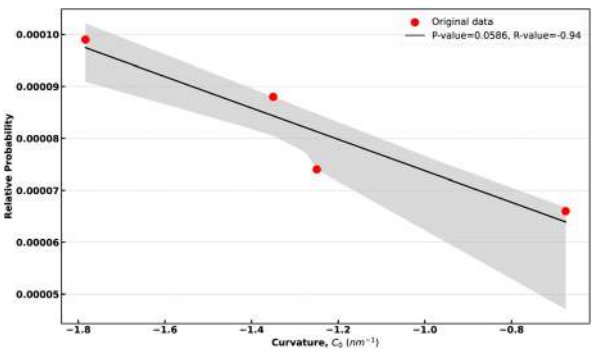

Fig. 8 Correlation between induced curvature (C_0) and relative probability ($f_{\tau\phi}$). The data show an inverse relationship (R-value = −0.94, P-value = 0.0586), with the shaded area representing the 95% confidence interval. The red data points correspond to original values from different models, and the black line represents the linear regression fit.

and strong electrostatic interactions with basic protein regions are widely recognized for its crucial roles in various membrane-related cellular processes, including protein recruitment and curvature induction.[31,32]

Electrostatic sequestration between PIP2 lipids and positively charged motifs of the protein induces phase separation within the membrane. This phenomenon exemplifies another type of nature's biophysical 'cheap trick',[34] facilitating complex molecular rearrangements with minimal energy expenditure.

Our findings are consistent with extensive coarse-grained simulations of complex lipid bilayers, which have demonstrated a direct correlation between lipid clustering (including PIP2 enrichment in the concave regions of the intracellular leaflet) and local membrane curvature, reinforcing the validity of lipid-driven membrane shaping mechanisms observed with the MARTINI force field.[58]

Consequently, longer PIP2 lipids accumulate at the protein's corners (corresponding to the vertices of an equilateral triangle where absorbent points or charged membrane-binding motifs are located), while the central region of the protein trimer becomes depleted of PIP2 (Fig. 9). This region, in turn, becomes enriched with shorter lipids such as POPC and POPE, forming distinct domains. Such differential lipid distribution could be a key driver of membrane curvature. This phenomenon can be visually observed in Fig. 9, which presents a topographic view of the membrane, color-coded to show PIP2 lipids (magenta) and protein myristoylate tails (green). As observed in Fig. 9, regions of elevated membrane levels are shown in purple, and these regions are also enriched with PIP2 lipids. Conversely, regions of lower membrane levels are shown in white and exhibit a lower concentration of PIP2. Notably, the presence of the protein complex leads to the depletion of PIP2 in the membrane region interacting with the protein's central area and the corresponding enrichment of PIP2 in the peripheral regions surrounding the protein; this is clearly visualized in the figure.

The resulting membrane domains differ in molecular properties, including the thickness of the hydrophobic region. The height difference between these lipid domains resembles a step or bridge (Fig. 11A). This step exposes the hydrophobic parts of the longer lipids to the aqueous environment, which is energetically unfavorable. To mitigate this exposure, boundary lipids adjust by altering their orientations and lengths, effectively stretching or shrinking to cover the exposed hydrophobic regions, as shown in Fig. 11B.[66,67] In this figure, two domains interact: one with taller lipids (black heads) and one

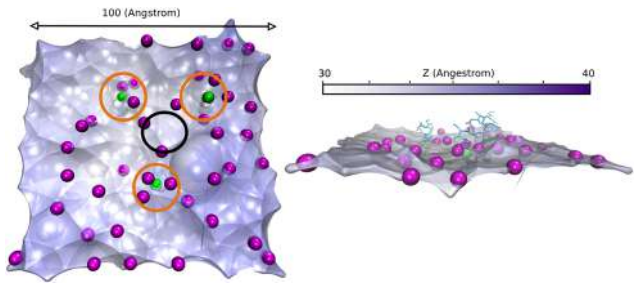

Fig. 9 Visualization of membrane topography, showing PIP2 lipids (magenta) and myristate tails (green). Purple areas indicate elevated membrane levels (greater *Z*-depth) that correlate with higher PIP2 concentrations, while white areas indicate lower membrane levels. This visualization demonstrates membrane deformation induced by PIP2 clustering and lipid sorting. The absorbing points are shown with orange circles and the central region with the black one.

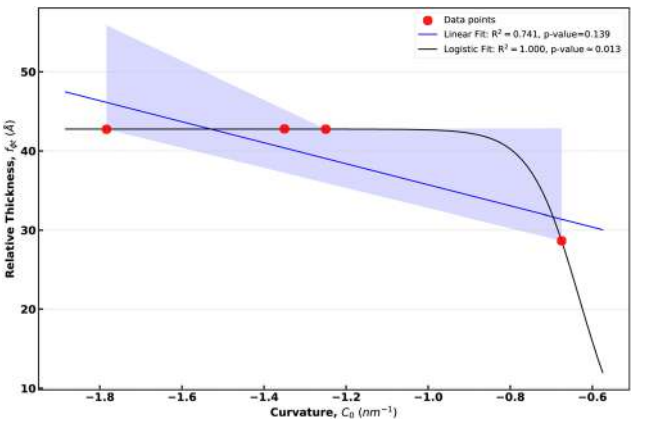

Fig. 10 Relationship between induced membrane curvature and relative membrane thickness across protein models (I–V). Data points (red circles) represent measurements for models I–V. The black line shows the logistic regression fit to the data (R^2 = 1.000, p-value ≈ 0.013). For comparison, the blue line shows the linear regression fit (R^2 = 0.741, p-value ≈ 0.139). Curvature (C_0) is given in units of nm^{-1} and relative thickness is presented in units of Å. The logistic model demonstrates a significantly better fit to the data (higher R^2 and a lower p-value) compared to the linear model, indicating a nonlinear relationship between induced membrane curvature and relative membrane thickness.

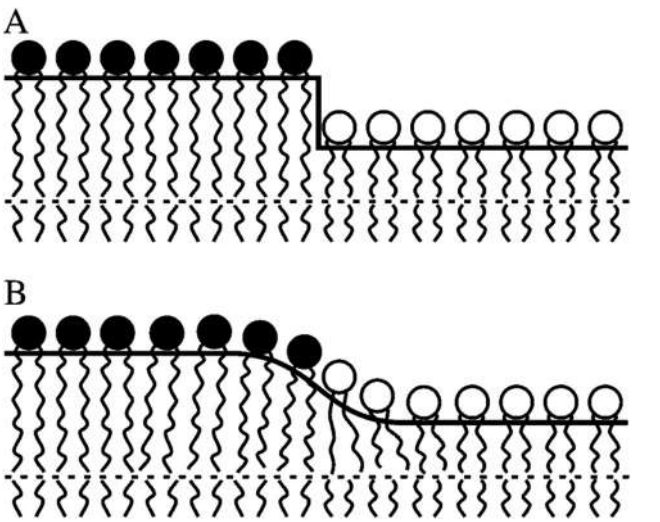

Fig. 11 (A) A lipid step leading to hydrophobic exposure at the boundary between taller and shorter lipids. (B) Adjustment of boundary lipids to cover the hydrophobic region, with the longer lipids compressing and shorter lipids stretching to form a gradual slope, mitigating hydrophobic exposure.[67]

with shorter lipids (white heads). In panel A, the abrupt boundary leads to potential hydrophobic exposure. In panel B, the shorter lipids stretch and the longer lipids compress, creating a gradual slope between the domains. This adaptation prevents direct hydrophobic exposure, maintaining membrane integrity. In a three-dimensional context, if this smooth transition occurs radially around a central point, it can result in an inward-curving cap-like structure. The taller lipids taper to align with the shorter lipids, forming a slope that converges inward, creating a cone-shaped structure with inward curvature.

Building upon our observation of PIP_2 enrichment, this lipid sorting process appears to create regions of differential membrane thickness – with PIP_2-rich areas potentially exhibiting increased thickness due to the larger PIP_2 headgroup and chain properties, and PIP_2-depleted regions thinning accordingly. To quantify this 'relative thickness', which we hypothesize is mechanistically coupled to curvature induction, we calculated the metric $f_{\phi t}$, defined as:

$$f_{\phi t} = \frac{\int \phi(x,y)t(x,y)\mathrm{d}x\mathrm{d}y}{\int \phi(x,y)\mathrm{d}x\mathrm{d}y}. \quad (3)$$

The relationship between induced curvature (C_0) and relative thickness ($f_{\phi t}$) across models I–IV is presented in Fig. 10. Although a linear fit reveals a weak correlation (R^2 = 0.741, p = 0.139), the logistic fit provides a significantly better fit, as indicated by a substantially higher R^2 value of 1.000 and a significantly lower p-value of 0.013. This nonlinear relationship suggests a threshold effect: at lower curvature values, relative thickness increases gradually, but beyond a critical curvature value, even small increments in curvature lead to a sharp rise in relative thickness. The decreasing trend in Fig. 10 strongly supports the role of PIP_2-driven lipid sorting and membrane thickness variations in curvature induction by protein trimers.

In the above explanation, it was assumed that three tails could successfully get inserted into the membrane, leading to a cap-like shape (Fig. 12A). However, as previously shown, except for model III, no other model could achieve this level of tail insertion. It is clear that when more than one leg is inserted into the membrane (as in models I, II, and IV), the membrane reshapes according to the described mechanism, resulting in a concave form or curvature induction (Fig. 12B).

The situation is notably different when only one leg is successfully inserted into the membrane, as seen in some replicas of model V. In this case, an uphill-like point forms near the leg insertion site, as only one absorption point is created, which is insufficient to produce a concave shape. For concavity to occur, at least two legs need to be inserted into the membrane.

It is also important to note that in model V, no electrostatic interaction is present at the N-terminus of the protein trimers. This model effectively serves as a crucial control, demonstrating the critical role of strong electrostatic interactions between the protein's highly basic region (HBR) and charged lipids like PIP2. The minimal tail insertion and curvature induction observed in model V, despite the presence of PIP2, underscore

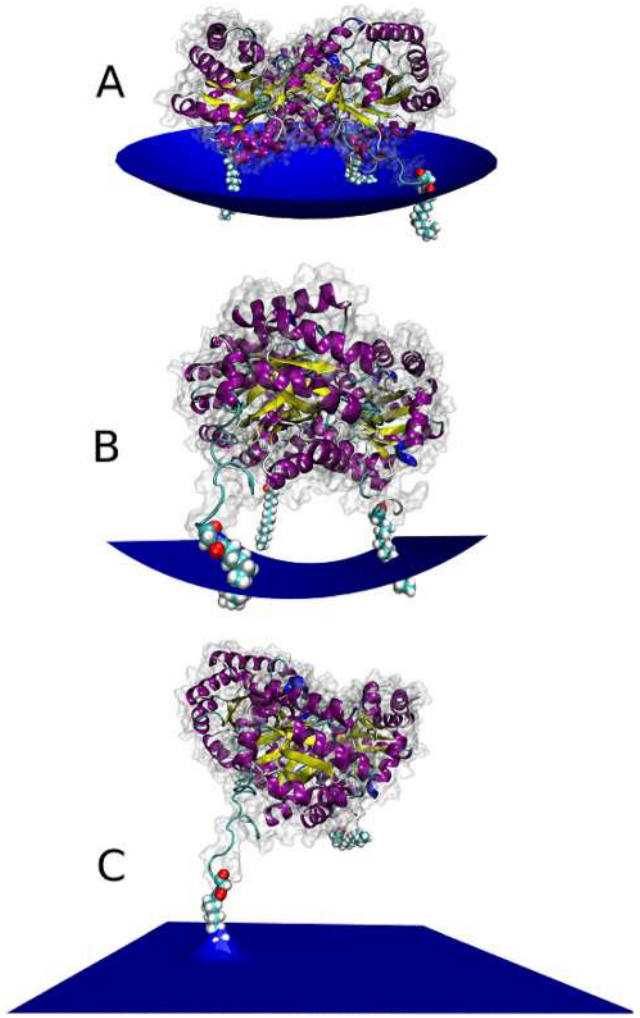

Fig. 12 The model illustrates the effect of protein tail stoichiometry on membrane curvature. (A) Insertion of multiple tails results in a relatively flat or slightly curved membrane. (B) Insertion of two tails induces a prominent concave membrane curvature. (C) Insertion of a single tail causes localized upward deformation at the insertion point, with minimal overall curvature.

that non-specific interactions or general lipid packing defects alone are insufficient to drive the robust curvature seen in other models. For further validation of PIP2's specific role, a control simulation with a membrane entirely lacking PIP2 (composed solely of POPC and POPE) was performed, yielding a significantly reduced curvature compared to model I (*e.g.*, $\langle C_0 \rangle = -0.41\ \mathrm{nm}^{-1}$, see Appendix A.6). According to the literature, proteins can successfully insert their lipid tails into the membrane when a large enough lipid packing defect is available.[68] The accumulation of PIP2 in certain regions may create these defects, allowing model V to insert its tail into the membrane.

Trajectory comparisons across various systems suggest that lipid tail insertion into the membrane initially reduces the lateral mobility of proteins on the membrane surface (Fig. 13). The methodology for calculating diffusion coefficients is

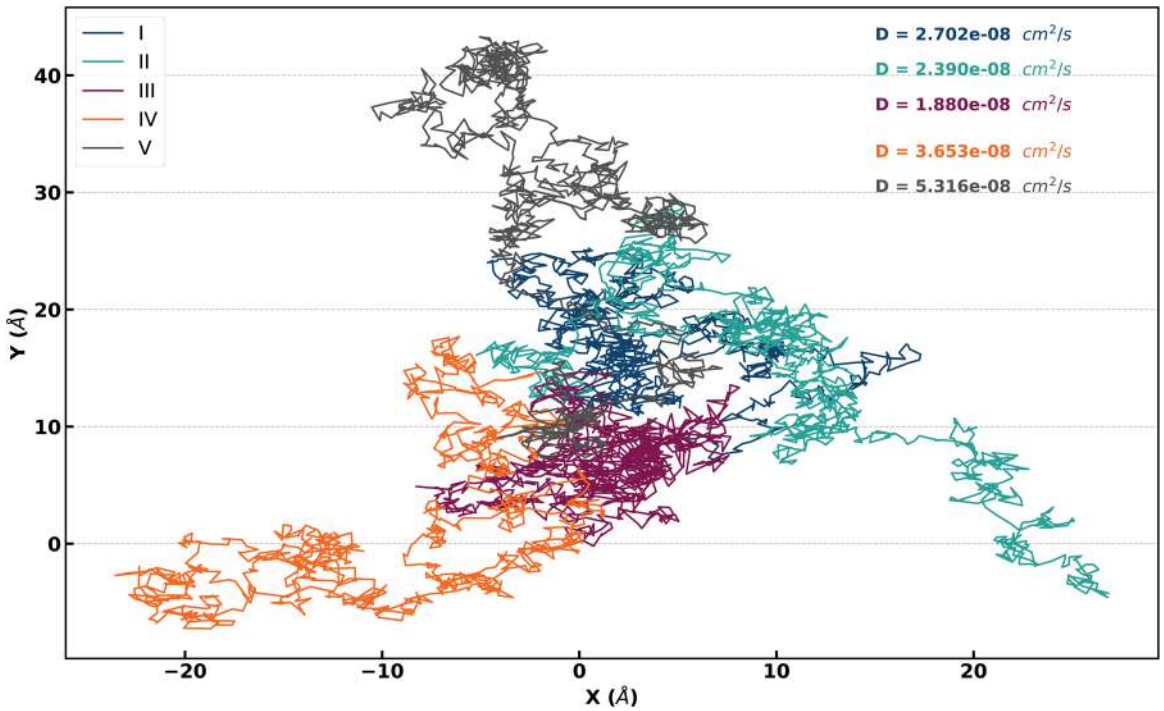

Fig. 13 Trajectories of trimeric protein movements on a two-dimensional lipid membrane surface. The paths for different models are shown, including I (dark blue), II (teal), III (purple), IV (orange), and V (black). Each trajectory depicts the spatial exploration in the *X*–*Y* plane (in angstroms, Å) over time. The diffusion coefficients (*D*) for each trimer are listed, indicating their relative rates of lateral movement on the membrane. These coefficients help illustrate the variability in membrane mobility across different trimer types.

detailed in Appendix A.2.6. Models with fewer lipid tails inserted (IV and V) exhibit greater protein mobility, reflected by higher diffusion coefficients ($D_{IV} = 3.65 \times 10^{-8}$ cm^2 S^{-1}, $D_V = 5.316 \times 10^{-8}$ cm^2 S^{-1}), while models I, II, and III show more restricted motion within the local lipid environment, corresponding to lower diffusion coefficients ($D_I = 2.702 \times 10^{-8}$ cm^2 S^{-1} > $D_{II} = 2.39 \times 10^{-8}$ cm^2 S^{-1} > $D_{III} = 1.88 \times 10^{-8}$ cm^2 S^{-1}).

Further investigation, combined with the probability distribution function (PDF) of the protein–membrane distance (Fig. 14), whose calculation methodology is detailed in Appendix A.2.6, reveals that lipid tail insertion also significantly decreases the distance between the protein platform and the membrane. This effect is especially pronounced in models with more than two lipid tails successfully integrated into the membrane. Specifically, in models I, II, and III, the distances are markedly reduced compared to models IV and V. According to Fig. 14, the distances for the first three models are 47.09, 47.05, and 47.08 Å, respectively, whereas in models IV and V, the distances are 47.82 and 53.28 Å, respectively.

Taken together, these results highlight the critical role of lipid tails in modulating the interaction between the protein's HBR and the charged lipids within the membrane. While electrostatic interactions bring the protein close to the membrane, the insertion of lipid tails reduces the protein's lateral mobility, allowing it to remain in a more confined local lipid environment. This immobilization acts as another type of biophysical 'cheap trick', reduction of dimensionality,[34] and provides sufficient time for charged lipids to migrate from other regions of the membrane and accumulate at the protein's HBR sites. As more lipids accumulate, electrostatic sequestration can occur, decreasing the average distance between the protein platform and the membrane and stabilizing the interaction between charged lipids and protein binding sites. This stabilization reinforces the protein–lipid complex and enhances the membrane curvature generation process.

Finally, our results reveal that these two mechanisms operate synergistically in a feedback loop (Fig. 15). The stronger the interaction in the highly basic region (HBR), the greater the likelihood of lipid tail insertion into the membrane. Increased lipid tail insertion reduces protein mobility, which in turn amplifies electrostatic interactions by allowing more charged lipids to accumulate around the protein. Additionally, lipid tails further strengthen these interactions by decreasing the average distance between the protein platform and the membrane, thereby reinforcing the protein–lipid complex. This mutual reinforcement promotes greater membrane curvature. The optimal performance is observed in model III, which exhibits the lowest diffusion coefficient and the shortest protein–membrane distance.

These results align with direct curvature measurements induced by this protein (Fig. 5), underscoring the cooperative role of the HBR and lipid tails in driving membrane curvature.

The elucidated mechanism by which each triangular trimer induces curvature provides insight into how the entire nano-

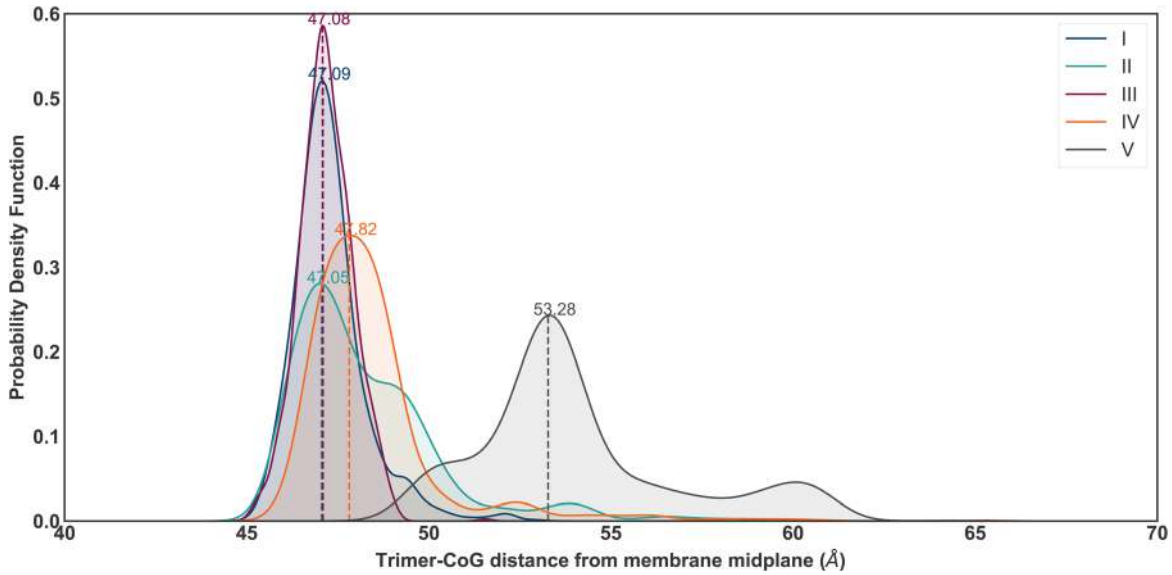

Fig. 14 Probability distribution function showing the distance between the center of geometry (CoG) of various trimer models and the membrane midplane (measured in angstroms, Å). The plot compares different models, including models I (dark blue), II (teal), III (purple), IV (orange), and V (black). The peak positions represent the most probable CoG distances for each model, with numerical labels indicating the specific distance values. This illustrates the differences in positioning among the various trimer models relative to the lipid membrane.

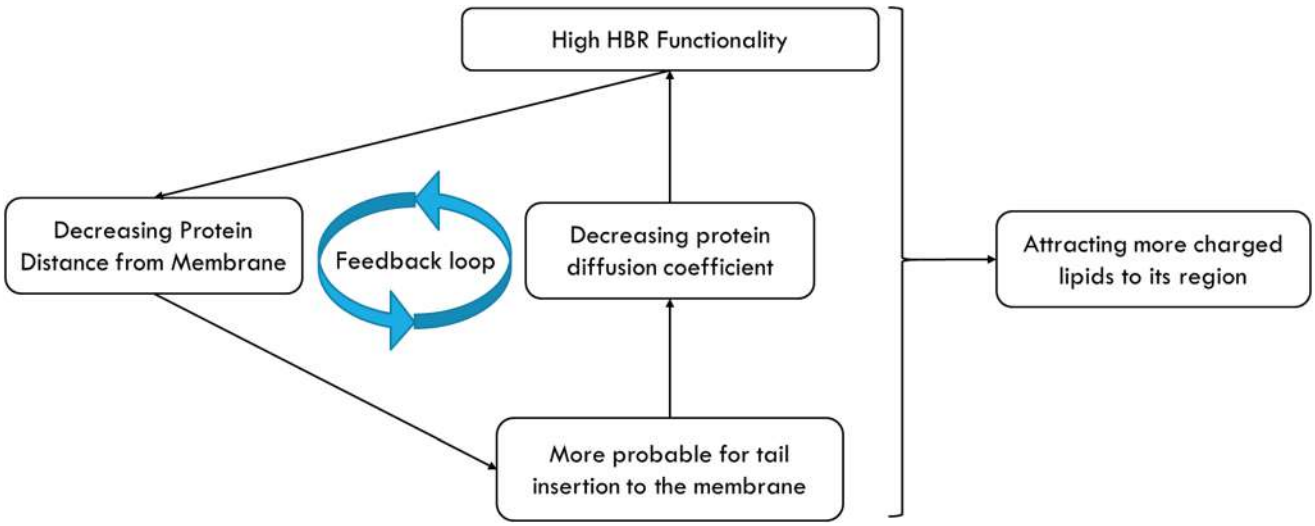

Fig. 15 Diagram illustrating the synergistic feedback loop driven by a high HBR (Highly Basic Region) and the lipid tails of trimers in inducing curvature in the lipid membrane. Strong electrostatic interactions in the highly basic region promote lipid tail insertion into the membrane, which reduces protein diffusion and mobility. This restricted mobility facilitates the accumulation of negatively charged lipids around the protein, further decreasing the distance between the protein and the membrane and reinforcing the protein–lipid complex. This mutual reinforcement amplifies protein–membrane interactions, leading to increased membrane curvature.

cage similarly imparts curvature to the membrane. Specifically, the arrangement of trimers in the nano-cage forms hollow pentagonal structures, with each trimer positioned at an angle of 58.3 degrees relative to its landing plane (Fig. 1A). This configuration places attraction points at the vertices of these pentagons. Since the rigidity of the nano-cage is higher than that of the membrane, it is assured that this mechanism effectively induces curvature in the membrane without causing any bending within the nano-cage itself.

The results from our models demonstrate that an increase in electrostatic interaction energy at the N-terminal significantly enhances the protein trimer's efficiency in inducing membrane curvature, which, at the experimental scale, translates to higher efficiency in the production of vesiculated nanocages. Notably, these findings are consistent with experimental data reported in the literature.[14] For instance, studies have shown that substituting the sequence of the HIV-1 Gag protein in the membrane domain, which has a release efficiency of

13%, with those from the MARCKS protein reduces the vesicle release efficiency to 5%. Conversely, substituting these amino acids with the PH domain from PLC_δ enhances it to 15%.

Theoretical predictions align with these experimental results, suggesting that increasing the charge in the membrane-binding domain of the PLC_δ-PH model to +4, compared to +2 in the HIV-1 Gag model, enhances release efficiency. In the MARCKS model, although its protein's effector domain carries a high charge of +13 (as shown in Fig. 16), it readily detaches from the membrane in the presence of Ca^{++}/calmodulin or upon phosphorylation of three serine residues by PKC.[34] This detachment weakens its interaction with the membrane, subsequently reducing curvature induction. Similarly, in model IV, the presence of a second tail disrupts the membrane interaction of the binding domain, leading to a decrease in curvature generation efficiency.

Overall, the strong agreement between our simulations and experimental observations reinforces the validity of our findings and provides deeper insights into the biophysical mechanisms underlying these interactions.

With the mechanism of curvature induction now clarified, it remains essential to determine the specific contribution of each trimeric triangle's interaction with the membrane to the total energy required for nano-cage vesiculation.

For this purpose, PMFs were further reconstructed from extensive MD simulations using Jarzynski's method. The distance between the protein platform (excluding its non-structural N-terminal region) and the mid-plane of the membrane is used as the reaction coordinate (Fig. 17). For model I, a plateau is observed in the PMF plot at a distance of approximately 65 Å, corresponding to an energy cost of around 280 kcal mol^{-1} (see Fig. 17). At this point, the detachment of one lipid tail occurs concurrently with the separation of the protein core from the membrane.

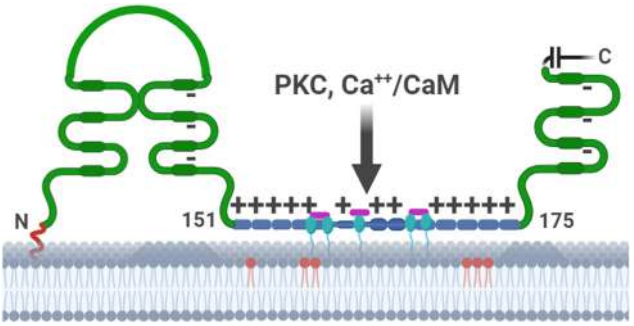

Fig. 16 Illustration of MARCKS bound to a lipid bilayer. The myristoyl group (shown in red) integrates into the membrane through hydrophobic interactions, while the 13 basic residues (depicted in blue) in the effector domain interact with acidic lipids, represented by 6 red circles indicating PIP_2. Additionally, five phenylalanine residues (depicted in cyan) are embedded in the bilayer. Phosphorylation of the three serine residues (highlighted in purple) by PKC or the binding of Ca^{++}/calmodulin leads to the displacement and detachment of the effector domain from the bilayer. Inspired by ref. 34.

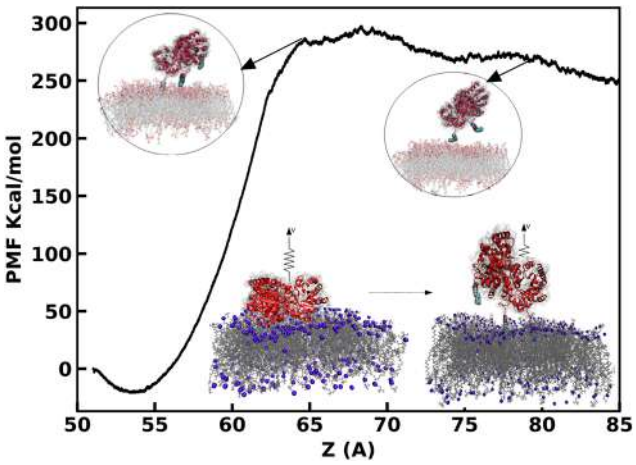

Fig. 17 Potential of mean force (PMF) profile for the detachment of the protein from the membrane along the Z-axis for model I. The PMF rises sharply as the protein core begins to separate from the membrane, reflecting the high energy required to overcome van der Waals and electrostatic interactions. The peak in the PMF corresponds to the detachment of the protein core and initial extraction of lipid tails. The insets illustrate key stages in the detachment process, showing shifts in the protein position and membrane interaction. The gradual decline in PMF after the peak indicates the completion of lipid tail extraction and the protein's release from membrane constraints. A conceptual discussion regarding the implications of this PMF in the broader context of vesiculation energetics and factors influencing encapsulation efficiency is provided in Appendix A.5.

Further progression of the process led to a decrease in the PMF, indicating that less energy is required to detach the remaining lipid tails compared to the protein core. At a distance of approximately 80 Å, all three lipid tails had fully dissociated from the lipid membrane. The energy data suggest that each trimer binding to the membrane contributes around 280 kcal mol^{-1}, facilitating membrane curvature.

This binding energy can be compared with the estimated energy required for vesiculation, calculated using the Helfrich Hamiltonian:[69]

$$E = \frac{1}{2}\kappa\left(\frac{1}{R_1}+\frac{1}{R_2}\right)^2, \quad (4)$$

where R_1 and R_2 represent the local radii of curvature and κ denotes the bending modulus of the membrane. For a typical phospholipid bilayer, κ is approximately $20k_BT$, with $k_BT \approx 4.1 \times 10^{-21}$ J ≈ 0.6 kcal mol^{-1}.[20]

Thus, the total energy required to form a spherical membrane vesicle of radius R can be estimated as:

$$8\pi\kappa \approx 500k_BT \approx 300 \text{ kcal mol}^{-1}. \quad (5)$$

Comparing these values reveals that each trimer binding to the membrane, providing approximately 280 kcal mol^{-1}, contributes nearly sufficient energy for vesiculation. Since the energy required to induce vesiculation is around 300 kcal mol^{-1}, a single trimer binding is almost enough to achieve this transformation. However, experimental results not only

support these estimations but also indicate that, on average, approximately 14 nanocages of type I are required to form a complete vesicle, underscoring the importance of collective, cooperative effects in real vesiculation. This apparent discrepancy highlights that the complex process of vesiculation is not solely dictated by the direct binding energy of individual proteins but rather involves a multitude of factors. As detailed in Appendix A.5 (eqn (10)), the overall aggregation energy of membrane remodeling encompasses not only bending energy but also entropic contributions from protein distribution, energy due to protein–protein aggregation, and compositional heterogeneity. A more detailed discussion on the theoretical considerations of this energy comparison, including the broader context of many-body effects and the comprehensive energetic landscape of membrane remodeling, is provided in Appendix A.5.

These experimental results indicate that an overly simplified application of the Helfrich Hamiltonian may not fully capture the complexity of this phenomenon. Numerous studies[69,70] have shown that the simultaneous interaction of multiple proteins with the membrane can induce additional forces between proteins, beyond the direct interaction forces they experience with the membrane itself. These additional forces arise due to local curvature generated within the membrane, effectively transmitting disturbances to more distant points. In this way, lipid membranes act as a medium that propagates localized deformations, much like electric fields mediate interactions between charges or the curvature of space–time mediates gravitational interactions. However, unlike these fields, the membrane-mediated field in this context is tangible and directly observable.

It is important to note that this study has focused on the mechanism of curvature induction at the level of individual protein trimers. Although our PMF calculation for model I provides a crucial energetic baseline, we have not yet addressed the potentially significant cooperative effects that may emerge from the simultaneous interaction of multiple nanocages with the membrane. Quantifying these cooperative effects and determining their influence on the overall energy landscape of vesiculation represent crucial directions for future investigations, particularly for understanding the collective behavior of nanocages in membrane remodeling and vesicle formation.

4. Conclusions

In recent years, synthetic protein nanocages have emerged as powerful tools in various fields, particularly in pharmaceuticals and medical applications. Inspired by the delivery mechanisms of viruses like HIV-1 and hepatitis, which efficiently transport genetic material to host cells, researchers have sought to replicate these strategies, transforming synthetic nanocages into functional artificial viruses. Our study provides insight into the molecular mechanisms underlying these transformations, offering a foundational understanding necessary for the optimal design of hybrid biological materials.

Achieving robust and effective nanocages necessitates a profound understanding of the molecular processes underlying vesiculation. Our molecular dynamics simulations elucidate these mechanisms, demonstrating that membrane curvature is predominantly triggered by the selective enrichment of longer lipids at the periphery of the protein–membrane interface, creating regions where the central area becomes relatively depleted of these specific lipids. This differential lipid distribution generates localized tension and curvature within the membrane, serving as a critical determinant for the formation of vesicular structures.

Our findings indicate that models possessing more potent highly basic regions (HBR) coupled with effective lipid-binding sites exhibited the highest capacity for inducing membrane curvature. This enhanced efficiency arises from a mutually reinforcing process: strong HBR–membrane interactions initially promote lipid tail insertion, which subsequently diminishes the protein's lateral mobility. This restricted movement, in turn, allows for a greater localized accumulation of negatively charged lipids around the protein, thereby reducing the average distance between the protein platform and the membrane. This stabilization significantly strengthens the protein–lipid complex, as evidenced particularly in models I through III.

Furthermore, our results highlight that even minor disruptions to lipid tail insertion – even in models with structurally similar HBRs – markedly impair the protein's capacity to induce membrane curvature. This emphasizes the critical need for a precisely coordinated interplay between the HBR and lipid tails for optimal curvature induction (*e.g.*, $C_{IV} < C_I$). These observations collectively point to a synergistic, stepwise feedback loop where the HBR and lipid-binding sites dynamically reinforce each other's functions, critically enabling the protein complex to efficiently shape the membrane, as visually summarized in Fig. 15.

The alignment of our simulation results with experimental data further validates our analysis, providing a reliable model for studying the molecular mechanisms involved in vesiculation. By measuring the binding energy of each protein trimer with the membrane, we quantified the contributions of each component of the nanocage to the energy required for vesiculation. We estimated a binding energy of approximately 280 kcal mol^{-1} per trimer, which, in theory, exceeds the energy necessary for vesiculation and the formation of a spherical lipid coating around the nanocage.

Under real biological conditions, where many proteins are present on the membrane surface, additional factors such as entropic forces from the membrane, alongside other present and known nanoscale forces, come into play, influencing the curvature formation process. Although these elements extend beyond the scope of the current study, they are essential for a complete understanding of membrane dynamics and will be addressed in future research. In subsequent work, we will explore how these forces impact protein packaging and the stability of vesicular structures, ultimately advancing our knowledge in the design of synthetic nanocages for biomedical applications.

While our study has focused on elucidating the fundamental molecular mechanism driven by specific protein–lipid interactions within a targeted, biologically relevant membrane environment, future work will systematically explore additional layers of complexity. This includes investigating the influence of other physiological membrane components, such as cholesterol, which can modulate membrane fluidity and protein interactions, and assessing the effects of varying protein densities and cooperative interactions on the overall curvature and vesiculation efficiency. We have also initiated control simulations with membranes entirely lacking PIP2 to further delineate its specific role, with preliminary results confirming its essential contribution to curvature induction (Appendix A.6).

Author contributions

S. R. conducted the simulations and data analysis and prepared all plots and figures for the manuscript. S. R. and M. R. E. conceived and designed the research project and jointly contributed to the interpretation of the results. S. R. drafted the main manuscript text. Both authors critically reviewed and approved the final manuscript.

Conflicts of interest

The authors declare that they have no conflicts of interest to disclose.

Data availability

The data that support the findings of this study are available from the corresponding author upon reasonable request. Computational models and simulation parameters used in this work can also be obtained upon request. All relevant data and analysis scripts used in this study are either included in the paper or its supplementary information (SI) or will be made available through a public repository upon request.

Appendix

A.1. General simulation equilibration

Ensuring that molecular dynamics simulations reach a stable, equilibrated state is crucial for the reliability of subsequent analyses. To confirm the stability and convergence of our simulated protein–membrane systems, we monitored the Root Mean Square Deviation (RMSD) of the protein backbone atoms relative to their initial minimized structures over the entire simulation duration. The RMSD serves as a key indicator of structural stability, reflecting how much the protein's conformation has deviated from its starting point. A plateau in the RMSD profile, coupled with a narrow distribution of RMSD values, typically indicates that the system has explored its accessible conformational space and reached a quasi-equilibrated state. Appendix Fig. 18 presents the RMSD profiles for all five protein models (I to V) over 200 ns of simulation, along with their corresponding probability density functions, demonstrating the successful equilibration of our systems prior to detailed analysis.

A.2. Analysis of simulation trajectories

To extract meaningful insights from our molecular dynamics simulations, several analytical procedures were employed. These methods allowed us to quantify key aspects of protein–membrane interaction, lipid dynamics, and membrane deformation.

A.2.1. Lipid tail insertion analysis. The number of inserted lipid tails (Fig. 4 in the main text) was quantified using a custom TCL script. For each trimer and frame, a tail was deemed inserted if the *Z*-coordinate of its terminal C4B bead was lower (deeper into the membrane) than the average *Z*-coordinate of the phosphate (PO4) headgroups of the membrane lipids. This method ensures that we count tails that have successfully penetrated beyond the polar headgroup region into the hydrophobic interior of the lipid bilayer, indicating effective membrane integration.

A.2.2. Curvature calculation methodology. To differentiate the curvature induced by the protein trimer from thermally-induced random deformations of the bilayer surface, we calculated the local curvature of the bilayer over time. The membrane surface was initially modeled by fitting the coordinates of the phosphorus beads of the lipids to a two-dimensional fifth-degree polynomial:

$$P(x,y) = \sum_{i=0}^{5} \sum_{j=0}^{5-i} a_{ij} x^i y^j. \tag{6}$$

Here, the outer sum iterates over the power i of x from 0 to 5 and the inner sum iterates over the power j of y from 0 to $5 - i$, ensuring that the total degree $i + j$ does not exceed 5. The coefficients a_{ij} correspond to each term $x^i y^j$.

Since the surface lacks steep gradients and the induced curvature of the bilayer is minor (Fig. 6 in the main text), the mean curvature, $C(x, y)$, can be linearly approximated using the Laplacian of the height function, as described by the Monge equation:

$$C(x,y) = \nabla \cdot \left(\frac{\nabla z(x,y)}{\sqrt{1 + (\nabla z(x,y))^2}} \right) \approx \Delta z(x,y). \tag{7}$$

The local curvature per unit area beneath the protein trimer is then defined as:

$$C_0 = \frac{1}{A_p} \int_{A_p} C(x,y) \mathrm{d}x\mathrm{d}y \tag{8}$$

where A_p is the projected area of the trimer on the membrane surface. In this formulation, inward bending is represented by a positive C_0, while outward bending is indicated by a negative C_0.

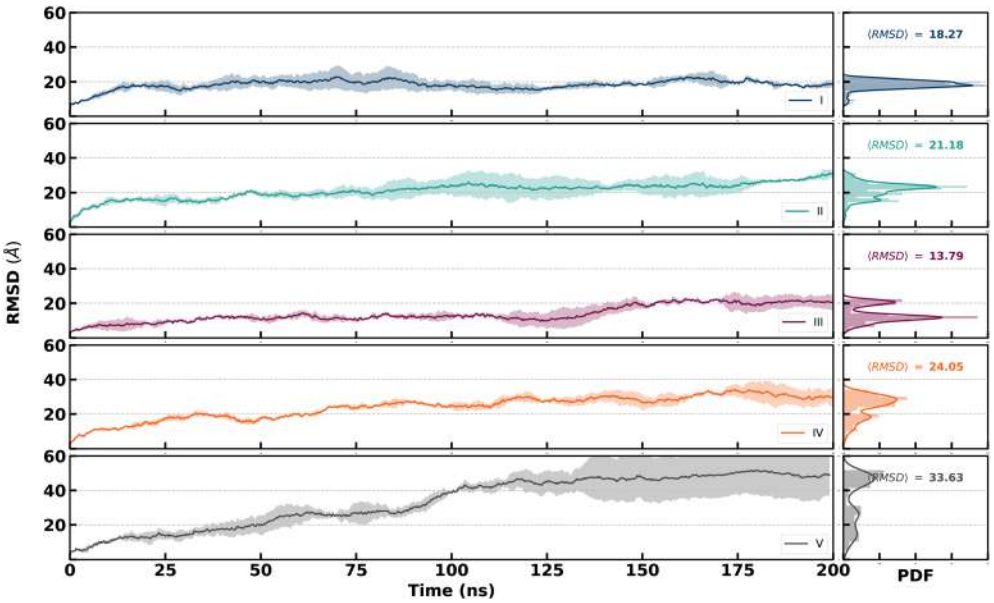

Fig. 18 RMSD variation of the models during 200 ns of simulation. Each plot shows the root mean square deviation (RMSD) over time for different models (I to V), with the corresponding probability density function (PDF) of the RMSD values shown on the right. The average RMSD (⟨RMSD⟩) is indicated for each model, highlighting the structural stability and variations observed across the simulations. Models I and III exhibit clear plateaus after approximately 100 ns, indicating that these structures have reached stable configurations. Model II also shows relatively minor fluctuations after 100 ns, suggesting that it is nearing equilibrium. For models IV and V, while there is a continuous increase in RMSD earlier in the simulation, both display plateau regions after around 175 ns, indicating that they may be approaching a more stable configuration toward the end of the simulation.

A.2.3. Detailed considerations for free energy calculations (Jarzynski's equality). Free energy calculations using Jarzynski's equality are a powerful approach for determining equilibrium free energy differences from non-equilibrium molecular dynamics simulations. This equality, $e^{-\beta\Delta F} = \langle e^{-\beta W} \rangle$, precisely relates the equilibrium free energy difference (ΔF) between two states to the ensemble average of the exponential of the non-equilibrium work (W) performed during transitions between these states.[71,72] This method is particularly advantageous for complex biomolecular systems as it circumvents the need for computationally demanding quasi-static (reversible) pathways. While the work values (W) measured in individual non-equilibrium trajectories typically exceed the free energy difference (ΔF), the exponential average correctly recovers the equilibrium value.

The practical application of Jarzynski's equality to biomolecular systems, especially for large and complex systems, necessitates careful parameter selection to ensure both computational feasibility and accuracy. As detailed by Park *et al.* (2003),[72] the choices of pulling velocity, force constant, and the number of sampled trajectories are critical for reliable free energy estimation.

A.2.3.1. Choice of pulling velocity and drag force subtraction. For biomolecules, the natural timescales of conformational changes or binding/unbinding events are often significantly longer than those accessible by conventional molecular dynamics simulations. Steered Molecular Dynamics (SMD) allows for the acceleration of these processes, inducing transitions at speeds higher than the quasi-static (reversible) regime (Park *et al.*, 2003).[72] While Jarzynski's equality theoretically holds for processes of any speed, its practical applicability and the convergence of the exponential average are greatly enhanced for "slow processes for which the fluctuation of work is comparable to the temperature" (Park *et al.*, 2003).[72]

Our chosen low pulling velocity of 0.0002 Å per timestep (equivalent to 0.1 nm ns^{-1} or 1 Å ns^{-1} based on a 2 fs timestep) was a deliberate balance. It is slow enough to *reduce* dissipated work and bring the system *closer* to the quasi-static regime, thereby improving the feasibility of the Jarzynski average, yet fast enough to be computationally tractable for biomolecular systems. As demonstrated in appendix Fig. 19, the protein's center of mass follows the dummy atom in a controlled manner, confirming the suitability of our pulling conditions for robust Jarzynski analysis (Fig. 20).

Crucially, to further refine our work measurements and account for inherent non-equilibrium effects, we adopted a sophisticated approach: we explicitly calculated and subtracted the hydrodynamic drag force from the total force exerted by the spring on the protein's center of mass. The drag force (F_{drag}) was estimated using Fick's law, approximated as $F_{\mathrm{drag}} = \zeta v$, where ζ is the drag coefficient (set to 800) and v is the instantaneous velocity of the protein's center of mass. This yielded the *net force* directly associated with the protein's interaction with the membrane and, subsequently, the *corrected net work* (W_{net}). This methodology allows us to isolate the free energy changes primarily associated with the binding/unbind-

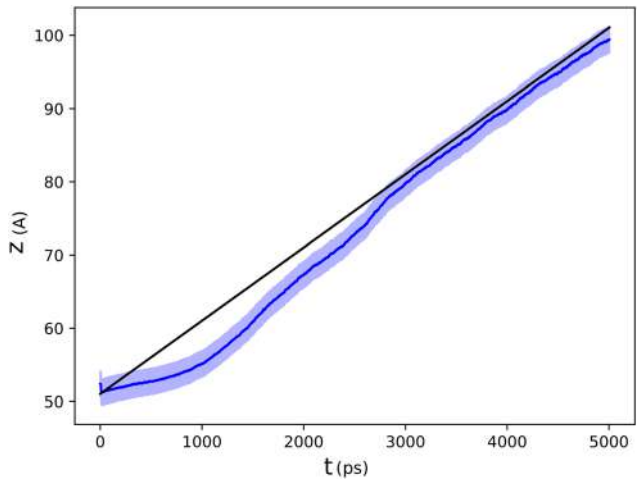

Fig. 19 Protein center of mass (COM) evolution relative to the dummy atom's position during steered molecular dynamics simulations, demonstrating the non-equilibrium nature of the pulling process while maintaining controlled system response for Jarzynski's analysis. Error bars (blue shadow) represent the standard deviation across the 10 independent trajectories.

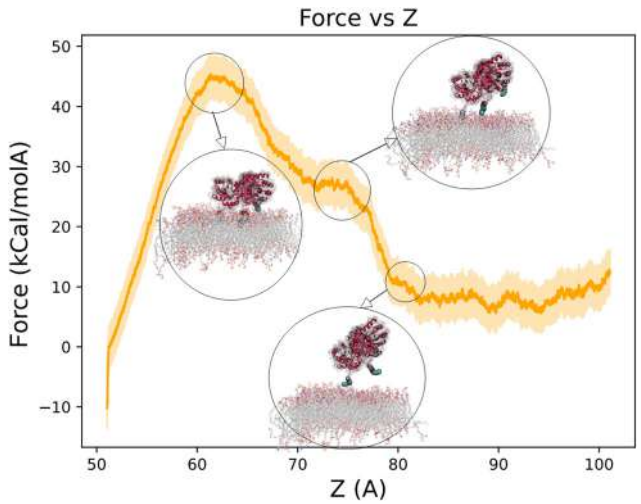

Fig. 20 Average net force exerted on the protein's center of mass as a function of reaction coordinate (Z). This net force is obtained after subtracting the calculated hydrodynamic drag force from the total force measured by the spring. The shaded region represents the standard deviation across the 10 independent trajectories, illustrating the magnitude of force fluctuations during the pulling process. The insets show representative snapshots of the protein–membrane system at different stages of the pulling pathway.

ing process, effectively mitigating a significant portion of the non-equilibrium artifacts arising from the solvent's resistance to protein movement. The PMF was then calculated using Jarzynski's equality on this corrected net work: $\Delta F = -k_B T \ln \langle e^{-W_{net}/k_B T} \rangle$.

A.2.3.2. Choice of force constant for the guiding potential. The potential of mean force (PMF) calculation relies on the "stiff spring approximation", which posits that the free energy of the system with an applied guiding potential (F) closely approximates the PMF of the original system ($\Phi \approx F$) when the force constant (k) of the spring is sufficiently large (Park *et al.*, 2003).[72] A large force constant ensures that the reaction coordinate (ξ) closely follows the constraint position (λ), thereby validating this approximation. Our chosen force constant of 7.5 kcal (mol A^2)$^{-1}$ was selected to be large enough to ensure this close adherence, which is crucial for the accuracy of the PMF. However, Park *et al.* (2003)[72] also cautioned against arbitrarily large force constants, as they can lead to increased fluctuations in the calculated PMF due to the large fluctuations of the external force. Therefore, our selection represents an optimized value that ensures the validity of the stiff spring approximation without introducing excessive statistical noise.

A.2.3.3. Number of trajectories and statistical convergence. A significant challenge in applying Jarzynski's equality, particularly when using the exponential average, is that the average is statistically dominated by rare trajectories corresponding to small work values (Park *et al.*, 2003).[72] Sampling these rare events accurately often requires a very large number of trajectories, which is computationally prohibitive for complex biomolecular systems.

To ensure robust statistical sampling and assess the convergence of our PMF calculation for model I, we performed 10 independent SMD runs. As illustrated in appendix Fig. 21, the corrected net work values obtained from these 10 trajectories still exhibit significant spread, indicating substantial residual work fluctuations even after drag subtraction. These fluctuations reflect the inherent heterogeneity of the unbinding pathways. While the direct exponential average was applied to

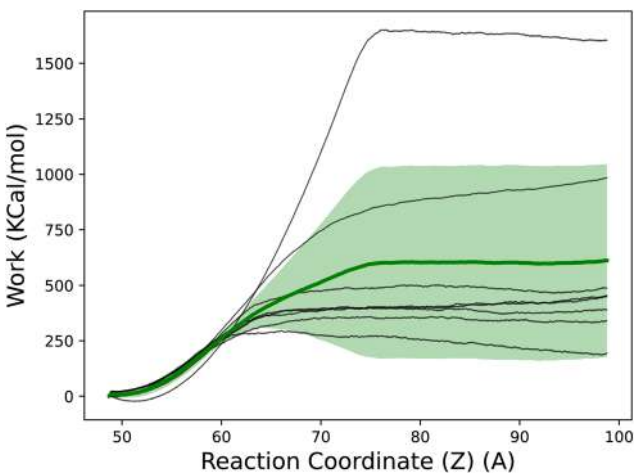

Fig. 21 Individual corrected net work trajectories as a function of reaction coordinate (Z). Each black line represents the accumulated work from one of the included independent SMD runs, after the subtraction of the hydrodynamic drag force. The green line represents the average corrected net work, with the shaded green region indicating the standard deviation across the trajectories. The significant spread and variability among these trajectories highlight the non-equilibrium nature of the individual pulling processes and the substantial residual work fluctuations, which are critical considerations for the statistical convergence of Jarzynski's equality.

this corrected net work, we acknowledge that for cases with very large work fluctuations relative to k_BT, the second-order cumulant expansion is often recommended for better accuracy with limited sampling (Park *et al.*, 2003).[72] However, our explicit subtraction of the dominant drag force component significantly enhances the reliability of the direct exponential average by reducing the overall magnitude of non-equilibrium work contributions. This approach, combined with our carefully selected pulling velocity and spring constant, ensures robust statistical sampling for reliable PMF estimation, considering the trade-off between computational cost and convergence accuracy for biomolecular systems. The robustness of this approach is further evidenced by the PMF profile's stability: as depicted in the figure, it remained consistent after incorporating six independent replicas. This empirical observation indicates that exponential averaging with six replicas yielded results identical to those obtained with all ten replicas, demonstrating early convergence despite the observed work fluctuations.

A discussion of the statistical convergence and limitations, particularly concerning the distribution of work values and the effectiveness of averaging schemes, is critical and has been considered in our analysis, aligning with the best practices for such calculations (Park *et al.*, 2003).[72]

A.2.4. Probability distribution functions and spatial correlations. Two-dimensional (2D) probability density maps were generated to analyze the spatial correlations between the protein's "membrane-binding motifs" and PIP2 lipids in the *XY* plane (Fig. 7 in the main text). This analysis involved extracting the x and y coordinates of the relevant beads (*e.g.*, protein HBR beads, PIP2 phosphate beads) from the simulation trajectories. A custom Python script was then used to process these data. First, Kernel Density Estimation (KDE) was applied to the 2D coordinate data points using the gaussian_kde function from the scipy.stats library to estimate the underlying probability density function. Subsequently, to create smooth, continuous density maps suitable for visualization and contour plotting, the calculated densities were interpolated onto a regular grid using the griddata function from scipy.interpolate with a cubic interpolation method. The resulting density maps visually represent regions of high and low probability for both PIP2 lipids and protein binding motifs, allowing for the identification of potential spatial correlations that could provide insights into the mechanisms of curvature induction.

A.2.5. Relative probability ($f_{\tau\phi}$) and relative thickness ($f_{\phi t}$) calculations. The metrics of "relative probability" ($f_{\tau\phi}$) and "relative thickness" ($f_{\phi t}$), as defined by their respective equations in the Results and discussion section of the main text, were calculated to quantify specific aspects of lipid–protein interactions. For $f_{\tau\phi}$, the spatial distributions $\tau(x, y)$ and $_{\phi}(x, y)$ were obtained from the 2D probability density maps (as described in Appendix A.2.4). The integrals were performed numerically over the discretized membrane grid using custom Python scripts. Similarly, for $f_{\phi t}$, the local membrane thickness $t(x, y)$ was determined by calculating the average Z-distance between the phosphate beads of the upper and lower leaflets within each grid cell for each frame. These numerical integrations were also carried out using custom Python scripts.

A.2.6. Diffusion coefficient and the protein–membrane distance. The lateral mobility of protein trimers on the membrane surface was determined by calculating their diffusion coefficients using the Einstein relation. This relation is expressed as:

$$\left\langle [\vec{r}_c(t) - \vec{r}_c(0)]^2 \right\rangle = 4Dt \tag{9}$$

where $\left\langle [\vec{r}_c(t) - \vec{r}_c(0)]^2 \right\rangle$ is the mean squared displacement (MSD) of the trimer's center of mass, D is the diffusion coefficient, and t is the time. The MSD was computed by averaging over every 100 consecutive time frames.

For the analysis of the protein–membrane distance, a custom TCL script (using VMD software) was employed to calculate the instantaneous distance between the center of geometry (CoG) of the protein trimer and the midplane of the membrane. The membrane midplane was determined from the average Z-coordinate of membrane beads for each simulation frame. The protein CoG was defined based on residues greater than 19 for chains A, B, and C to exclude specific N-terminal regions. The resulting time-series data of these distances were then processed using a Python script. This script was used to generate probability density functions (PDFs) of the protein–membrane distance (*e.g.*, as shown in Fig. 14 in the main text), thereby providing insights into the protein's vertical positioning relative to the bilayer. This involved reading the distance data and applying kernel density estimation (KDE) to smooth the distribution.

A.3. Rationale for lipid composition and the equilibration strategy

Our synthetic nanocages are designed with a membrane-binding domain identical to that of the HIV Gag polyprotein, which inspired our work. Given this precise biomimicry, it is exceedingly probable that our nanocages will interact with and target the same membrane microenvironments as the native Gag polyprotein. Experimental evidence[41] unequivocally demonstrates that HIV-1 Gag proteins do not randomly interact with the entire plasma membrane but rather exhibit a strong and preferential targeting to specific microdomains within the host cell membrane that are significantly enriched with PIP2 and cholesterol. Therefore, our chosen lipid composition, which explicitly mirrors the known composition of the HIV virus membrane, accurately represents these pre-existing, targeted, PIP2-enriched microdomains on the host cell membrane that are relevant to Gag's function. This approach constituted a deliberate and effective computational 'shortcut' in our simulation design. By directly initiating our simulations within this physiologically relevant, pre-enriched environment, we were able to efficiently focus our computational resources on dissecting the intricate molecular mechanisms that occur once the protein has arrived at its specific biological target site, thereby circumventing the need for computationally pro-

hibitive and biologically less relevant simulations required to observe the *de novo* formation of such specialized lipid domains from a dilute, globally averaged lipid mixture over extremely long timescales. Prior to combining, the membrane was individually equilibrated for 1 μs to ensure the formation of any intrinsic lipid clusters, followed by 0.5 μs of simulation with the protein, allowing ample time for protein-induced lipid reorganization and system equilibration.

A.4. Molecular mechanism of tail sequestration

This section details the molecular mechanism of lipid tail sequestration observed in model IV, where the second lipid tails interact non-productively with the protein instead of being inserted into the membrane. This internal sequestration, sometimes involving the tails being drawn into hydrophobic cavities, explains the reduced insertion efficiency in models IV and V (appendix Fig. 22).

A.5. Energetic landscape of membrane remodeling and vesiculation

The comparison between the calculated binding energy of a single trimer (280 kcal mol^{-1}) and the estimated Helfrich vesiculation energy of a small vesicle (300 kcal mol^{-1}) serves as a first-order energetic feasibility assessment. This approach is consistent with the established literature in membrane biophysics, including the work by Deserno and colleagues,[73] which explicitly states that "the energy needed for such large-scale changes in membrane geometry significantly exceeds the binding energy between individual proteins and between the protein and the membrane, and cooperative action is essential". Our finding that the binding energy of a single trimer is nearly sufficient, but not entirely, for the formation of a vesicle of a specific size directly supports the concept that multiple trimers must cooperate to achieve the required energy and induce stable vesiculation. Our study on individual trimers elucidates the fundamental molecular mechanisms that contribute to the overall cooperative process observed with the full nanocage.

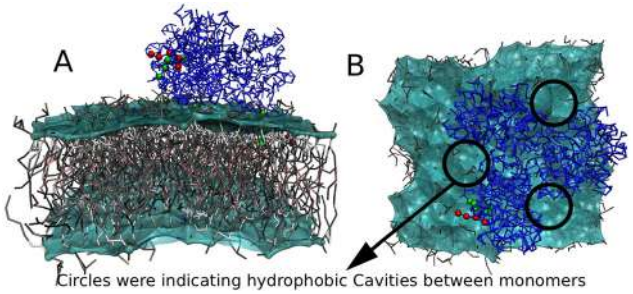

Fig. 22 Molecular mechanism of internal lipid tail sequestration in model IV. This figure illustrates the non-productive interaction of the second lipid tails with the protein in model IV, leading to their sequestration rather than membrane insertion. (A) Side view of a protein trimer (blue wireframe) interacting with the lipid membrane (cyan surface, with underlying lipid tails shown in the grey wireframe). The first lipid tails, which are associated with an electrostatic motif, are represented by red spheres, and the second lipid tails, which lack this motif, are shown as green spheres. This snapshot highlights how the green second lipid tails, instead of getting inserted into the membrane, become entangled with the red first tails and adhere to the external, hydrophobic surface of the protein. (B) Top-down view of the same system, further illustrating the self-association and protein-binding of the second lipid tails, which prevents their integration into the lipid bilayer. The black circles highlight hydrophobic cavities between monomers into which these non-inserted tails are often drawn. This internal sequestration mechanism, sometimes involving the tails being pulled into these inter-monomer pockets, explains the reduced insertion efficiency observed in models IV and V.

Furthermore, our theoretical framework acknowledges the multi-component nature of membrane remodeling energy. The total free energy associated with protein aggregation and membrane deformation includes various contributions, as described by equations similar to eqn (10), which considers bending energy, entropic contributions from protein distribution, and energy due to protein–protein aggregation and compositional heterogeneity.[74–76] In eqn (10), κ is the bending rigidity, H is the mean curvature, C is the spontaneous curvature, κ_G is the Gaussian bending modulus, K is the Gaussian curvature, T is the temperature, a is the area per lipid, ϕ is the local protein concentration, and J relates to protein–protein interactions and compositional heterogeneity. This comprehensive view underscores that the Helfrich estimate is a useful first-order approximation for the bending energy component, serving as a benchmark, but our understanding of the overall process extends to these more complex, collective phenomena. We have clarified this interpretation in the Results and discussion section.

$$W_{\text{Aggregation}} = \int_{\omega} \left(\underbrace{2\kappa(H-C)^2 + \kappa_G K}_{\text{Bending energy}} + \underbrace{\frac{T}{a^2}(\phi \ln \phi + (1-\phi)\ln(1-\phi))}_{\text{Energy entropy}} + \underbrace{\frac{J}{2a^2}\phi(1-\phi)}_{\text{protein aggregation due to energy}} + \underbrace{\frac{J}{4}(\nabla\phi)^2}_{\text{compositional heterogeneity}} \right) \mathrm{d}A \tag{10}$$

A.6. Control simulations with PIP2-free membranes

To further confirm the specific and critical role of PIP2 in inducing membrane curvature, we performed control simulations with a membrane entirely lacking PIP2. In these simulations, the membrane was composed solely of POPC and POPE lipids. The results from these control simulations demonstrated a significantly reduced capacity for curvature induction compared to model I (*e.g.*, $\langle C_0 \rangle = -0.41 \pm 0.02$ nm^{-1} for the PIP2-free membrane *vs.* $\langle C_0 \rangle = -1.18 \pm 0.05$ nm^{-1} for model I). This finding strongly supports our conclusion that the robust curvature observed in our main models is directly dependent on the presence of PIP2 lipids and the specific electrostatic interactions of PIP2 lipids with the protein's HBR,

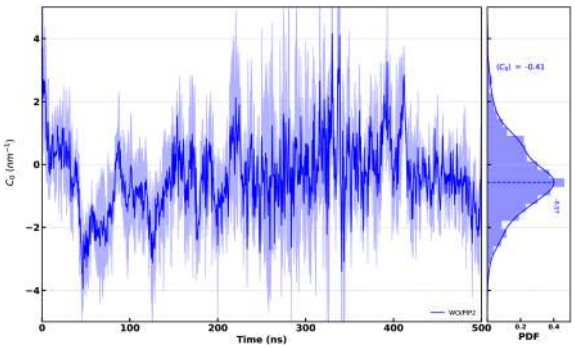

Fig. 23 Mean membrane curvature (C_0) over time for model I interacting with a PIP2-free membrane (composed solely of POPC and POPE lipids). The solid line represents the mean curvature calculated from three independent simulation replicas, with the shaded region indicating the standard error of the mean (SEM). The observed average curvature in the PIP2-free membrane ($\langle C_0 \rangle$ = −0.41 ± 0.02 nm^{-1}) is significantly reduced compared to model I interacting with a PIP2-enriched membrane ($\langle C_0 \rangle$ = −1.18 ± 0.05 nm^{-1}), thus confirming the essential role of PIP2 lipids and their electrostatic interactions in robust membrane curvature induction.

rather than generic membrane deformations or non-specific protein–lipid interactions (Fig. 23).

Acknowledgements

We are grateful to the HPC of SUT for providing the computational resources for this study.

References

1 L. A. Lee and Q. Wang, *Nanomedicine*, 2006, **2**, 137–149.
2 N. Ferrer-Miralles, E. Rodríguez-Carmona, J. L. Corchero, E. Garcia-Fruitos, E. Vázquez and A. Villaverde, *Crit. Rev. Biotechnol.*, 2015, **35**, 209–221.
3 M. Flenniken, M. Uchida, L. Liepold, S. Kang, M. J. Young and T. Douglas, *Viruses and Nanotechnology*, 2009, pp. 71–93.
4 M. Uchida, M. T. Klem, M. Allen, P. Suci, M. Flenniken, E. Gillitzer, Z. Varpness, L. O. Liepold, M. Young and T. Douglas, *Adv. Mater.*, 2007, **19**, 1025–1042.
5 N. M. Molino and S.-W. Wang, *Curr. Opin. Biotechnol.*, 2014, **28**, 75–82.
6 B. Sana, E. Johnson and S. Lim, *Biochim. Biophys. Acta, Gen. Subj.*, 2015, **1850**, 2544–2551.
7 E. Vázquez and A. Villaverde, *Microb. Cell Fact.*, 2010, **9**, 1–4.
8 Y.-T. Lai, N. P. King and T. O. Yeates, *Trends Cell Biol.*, 2012, **22**, 653–661.
9 Y.-T. Lai, K.-L. Tsai, M. R. Sawaya, F. J. Asturias and T. O. Yeates, *J. Am. Chem. Soc.*, 2013, **135**, 7738–7743.
10 J. B. Bale, S. Gonen, Y. Liu, W. Sheffler, D. Ellis, C. Thomas, D. Cascio, T. O. Yeates, T. Gonen, N. P. King, *et al.*, *Science*, 2016, **353**, 389–394.
11 Y. Hsia, J. B. Bale, S. Gonen, D. Shi, W. Sheffler, K. K. Fong, U. Nattermann, C. Xu, P.-S. Huang, R. Ravichandran, *et al.*, *Nature*, 2016, **535**, 136–139.
12 T. O. Yeates and J. E. Padilla, *Curr. Opin. Struct. Biol.*, 2002, **12**, 464–470.
13 S. Bhaskar and S. Lim, *NPG Asia Mater.*, 2017, **9**, e371.
14 J. Votteler, C. Ogohara, S. Yi, Y. Hsia, U. Nattermann, D. M. Belnap, N. P. King and W. I. Sundquist, *Nature*, 2016, **540**, 292–295.
15 R. Flores, S. Gago-Zachert, P. Serra, R. Sanjuán and S. F. Elena, *Annu. Rev. Microbiol.*, 2014, **68**, 395–414.
16 P. Forterre and M. Krupovic, *Viruses: essential agents of life*, Springer, 2012, pp. 43–60.
17 E. V. Koonin, *Philos. Trans. R. Soc., B*, 2016, **371**, 20150442.
18 L. L. Lanier, *Nat. Rev. Immunol.*, 2008, **8**, 259–268.
19 T. G. Edwardson and D. Hilvert, *J. Am. Chem. Soc.*, 2019, **141**, 9432–9443.
20 B. J. Reynwar, G. Illya, V. A. Harmandaris, M. M. Müller, K. Kremer and M. Deserno, *Nature*, 2007, **447**, 461–464.
21 M. Simunovic, A. Srivastava and G. A. Voth, *Proc. Natl. Acad. Sci. U. S. A.*, 2013, **110**, 20396–20401.
22 W. Pezeshkian and J. H. Ipsen, *Soft Matter*, 2019, **15**, 9974–9981.
23 J. Midya, T. Auth and G. Gompper, *ACS Nano*, 2023, **17**, 1935–1945.
24 A. H. Bahrami, R. Lipowsky and T. R. Weikl, *Phys. Rev. Lett.*, 2012, **109**, 188102.
25 M. Sadeghi, *Soft Matter*, 2022, **18**, 3917–3927.
26 T. Yue, S. Li, X. Zhang and W. Wang, *Soft Matter*, 2010, **6**, 6109–6118.
27 K. Jaskiewicz, A. Larsen, D. Schaeffel, K. Koynov, I. Lieberwirth, G. Fytas, K. Landfester and A. Kroeger, *ACS Nano*, 2012, **6**, 7254–7262.
28 Y. Li, M. Kröger and W. K. Liu, *Nanoscale*, 2015, **7**, 16631–16646.
29 K. A. Smith, D. Jasnow and A. C. Balazs, *J. Chem. Phys.*, 2007, **127**, 084703.
30 T. Yue and X. Zhang, *ACS Nano*, 2012, **6**, 3196–3205.
31 H. T. McMahon and J. L. Gallop, *Nature*, 2005, **438**, 590–596.
32 J. Zimmerberg and M. M. Kozlov, *Nat. Rev. Mol. Cell Biol.*, 2006, **7**, 9–19.
33 K. Schmidt-Nielsen, *How animals work*, Cambridge University Press, 1972.
34 S. McLaughlin, J. Wang, A. Gambhir and D. Murray, *Annu. Rev. Biophys. Biomol. Struct.*, 2002, **31**, 151–175.
35 B. Webb and A. Sali, *Curr. Protoc. Bioinf.*, 2016, **54**, 5–6.
36 E. F. Pettersen, T. D. Goddard, C. C. Huang, G. S. Couch, D. M. Greenblatt, E. C. Meng and T. E. Ferrin, *J. Comput. Chem.*, 2004, **25**, 1605–1612.
37 W. Humphrey, A. Dalke and K. Schulten, *J. Mol. Graphics*, 1996, **14**, 33–38.
38 J. K. Ousterhout, *Tcl and the Tk Toolkit*, Boston, MA, 1994.

39 R. Anandakrishnan, B. Aguilar and A. V. Onufriev, *Nucleic Acids Res.*, 2012, **40**, W537–W541.
40 S. Jo, T. Kim, V. G. Iyer and W. Im, *J. Comput. Chem.*, 2008, **29**, 1859–1865.
41 A. Alfadhli, R. L. Barklis and E. Barklis, *Virology*, 2009, **387**, 466–472.
42 S. J. Marrink, A. H. De Vries and A. E. Mark, *J. Phys. Chem. B*, 2004, **108**, 750–760.
43 S. J. Marrink, H. J. Risselada, S. Yefimov, D. P. Tieleman and A. H. De Vries, *J. Phys. Chem. B*, 2007, **111**, 7812–7824.
44 A. Y. Shih, A. Arkhipov, P. L. Freddolino and K. Schulten, *J. Phys. Chem. B*, 2006, **110**, 3674–3684.
45 L. Monticelli, S. K. Kandasamy, X. Periole, R. G. Larson, D. P. Tieleman and S. J. Marrink, *J. Chem. Theory Comput.*, 2008, **4**, 819–834.
46 D. H. De Jong, G. Singh, W. F. D. Bennett, C. Arnarez, T. A. Wassenaar, L. V. Schafer, X. Periole, D. P. Tieleman and S. J. Marrink, *J. Chem. Theory Comput.*, 2013, **9**, 687–697.
47 A. Arkhipov, Y. Yin and K. Schulten, *Biophys. J.*, 2008, **95**, 2806–2821.
48 L. Charlier, M. Louet, L. Chaloin, P. Fuchs, J. Martinez, D. Muriaux, C. Favard and N. Floquet, *Biophys. J.*, 2014, **106**, 577–585.
49 P. J. Stansfeld, R. Hopkinson and M. S. P. Sansom, *Biochemistry*, 2009, **48**, 10926–10933.
50 G. van den Bogaart, K. Meyenberg and R. Jahn, *Nature*, 2011, **479**, 552–555.
51 J. C. Phillips, R. Braun, W. Wang, J. Gumbart, E. Tajkhorshid, E. Villa, C. Chipot, R. D. Skeel, L. Kale and K. Schulten, *J. Comput. Chem.*, 2005, **26**, 1781–1802.
52 A. C. Stark, C. T. Andrews and A. H. Elcock, *J. Chem. Theory Comput.*, 2013, **9**, 4176–4185.
53 P. J. Stansfeld, E. E. Jefferies and M. S. Sansom, *Structure*, 2012, **21**, 810–819.
54 C. Arnarez, J.-P. Mazat, J. Elezgaray, S. J. Marrink and X. Periole, *J. Am. Chem. Soc.*, 2013, **135**, 3112–3120.
55 E. Psachoulia, P. J. Bond, P. W. Fowler and M. S. Sansom, *Biochemistry*, 2008, **47**, 10503–10512.
56 A. Kalli, B. A. Hall, and M. S. Sansom, *Structure*, 2011, **19**, 1477–1484.
57 X. Periole, A. M. Knepp, T. P. Sakmar, S. J. Marrink and T. Huber, *J. Am. Chem. Soc.*, 2012, **134**, 10959–10965.
58 H. Koldsø, D. Shorthouse, J. Hélie and M. S. Sansom, *PLoS Comput. Biol.*, 2014, **10**, e1003911.
59 A. Y. Shih, L. Freddolino, S. G. Sligar and K. Schulten, *Nano Lett.*, 2007, **7**, 1692–1696.
60 K. Vanommeslaeghe, E. Hatcher, C. Acharya, S. Kundu, S. Zhong, J. Shim, E. Darian, O. Guvench, P. Lopes, I. Vorobyov, *et al.*, *J. Comput. Chem.*, 2010, **31**, 671–690.
61 A. Bernardin, H. Chen, J. R. Comer, G. Fiorin, H. Fu, J. Hénin, A. Kohlmeyer, F. Marinelli, J. V. Vermaas and A. D. White, Collective variables module reference manual for lammps, 2013.
62 C. Jarzynski, *Phys. Rev. Lett.*, 1997, **78**, 2690.
63 R. B. Gennis, *Biomembranes: molecular structure and function*, Springer Science & Business Media, 2013.
64 J. P. Bradshaw, R. J. Bushby, C. C. Giles and M. R. Saunders, *Biochemistry*, 1999, **38**, 8393–8401.
65 C. Zhou, V. Garigapati and M. F. Roberts, *Biochemistry*, 1997, **36**, 15925–15931.
66 E. Schäffer and U. Thiele, *Eur. Phys. J. E:Soft Matter Biol. Phys.*, 2004, **14**, 169–175.
67 P. I. Kuzmin, S. A. Akimov, Y. A. Chizmadzhev, J. Zimmerberg and F. S. Cohen, *Biophys. J.*, 2005, **88**, 1120–1133.
68 V. Monje-Galvan and G. A. Voth, *eLife*, 2020, **9**, e58621.
69 M. Deserno, K. Kremer, H. Paulsen, C. Peter and F. Schmid, *Computational studies of biomembrane systems: theoretical considerations, simulation models, and applications*, Springer, 2014.
70 M. Deserno, See https://www.cmu.edu/biolphys/deserno/pdf/membrane_theory.pdf, 2007.
71 C. Jarzynski, *Phys. Rev. Lett.*, 1997, **78**, 2690–2693.
72 S. Park, F. Khalili-Araghi, E. Tajkhorshid and K. Schulten, *Phys. Rev. E:Stat., Nonlinear, Soft Matter Phys.*, 2003, **67**, 051907.
73 B. J. Reynwar, G. Illya, V. A. Harmandaris, M. M. Müller, K. Kremer and M. Deserno, *Nature*, 2007, **447**, 461–464.
74 M. Simunovic, G. A. Voth and R. Lipowsky, *Nano Lett.*, 2016, **16**, 3137–3142.
75 Z. Shi, T. Baumgart and D. E. Discher, *Phys. Rev. Lett.*, 2014, **113**, 238101.
76 M. Alimohamadi, M. R. Ejtehadi and R. Khosravi, *J. Phys. Chem. B*, 2018, **122**, 4443–4454.